

University of Nebraska - Lincoln

DigitalCommons@University of Nebraska - Lincoln

Mechanical (and Materials) Engineering --
Dissertations, Theses, and Student Research

Mechanical & Materials Engineering,
Department of

1-2020

On Geometric Design Rules and In-Process Build Quality Monitoring of Thin-Wall Features Made Using Laser Powder Bed Fusion Additive Manufacturing Process

Aniruddha Gaikwad

University of Nebraska - Lincoln, aniruddha.gaikwad@huskers.unl.edu

Follow this and additional works at: <https://digitalcommons.unl.edu/mechengdiss>



Part of the [Materials Science and Engineering Commons](#), and the [Mechanical Engineering Commons](#)

Gaikwad, Aniruddha, "On Geometric Design Rules and In-Process Build Quality Monitoring of Thin-Wall Features Made Using Laser Powder Bed Fusion Additive Manufacturing Process" (2020). *Mechanical (and Materials) Engineering -- Dissertations, Theses, and Student Research*. 151.
<https://digitalcommons.unl.edu/mechengdiss/151>

This Article is brought to you for free and open access by the Mechanical & Materials Engineering, Department of at DigitalCommons@University of Nebraska - Lincoln. It has been accepted for inclusion in Mechanical (and Materials) Engineering -- Dissertations, Theses, and Student Research by an authorized administrator of DigitalCommons@University of Nebraska - Lincoln.

ON GEOMETRIC DESIGN RULES AND IN-PROCESS BUILD QUALITY
MONITORING OF THIN-WALL FEATURES MADE USING
LASER POWDER BED FUSION ADDITIVE MANUFACTURING PROCESS

by

Aniruddha Gaikwad

A THESIS

Presented to the Faculty of
The Graduate College at the University of Nebraska
In Partial Fulfillment of Requirements
For the Degree of Master of Science
Major: Mechanical Engineering & Applied Mechanics

Under the Supervision of Professor Prahalada Rao.

Lincoln, Nebraska

January, 2019

ON GEOMETRIC DESIGN RULES AND IN-PROCESS BUILD QUALITY
MONITORING OF THIN-WALL FEATURES MADE USING
LASER POWDER BED FUSION ADDITIVE MANUFACTURING PROCESS

Aniruddha Gaikwad, M.S.

University of Nebraska, 2019

Advisor: Prahalada Rao

The goal of this thesis is to quantify the link between the design features (geometry), in-process signatures, and build quality of parts made using the laser powder bed fusion (LPBF) additive manufacturing (AM) process. This knowledge is the foundational basis for proposing design rules in AM, as well as for detecting the impending build failures using in-process sensor data.

As a step towards this goal, the objectives of this work are two-fold:

- 1) Quantify the effect of the geometry and orientation on the build quality of thin-wall features. To explain further, the geometry related factor is the ratio of the length of a thin wall (l) to its thickness (t) in the X-Y plane along which powder is deposited (raked or rolled), termed as the aspect ratio (length-to-thickness ratio, l/t), and the angular orientation (θ) of the part which refers to the inclination of the part in the X-Y plane to the re-coater of the LPBF machine.
- 2) Monitor the thin-wall build quality by analyzing the images of the part obtained from an in-process optical camera using a convolutional neural network.

To realize these objectives, we designed a test part with a set of thin-wall features (fins) with varying aspect ratios from Titanium alloy (Ti-6Al-4V) material – the aspect

ratio l/t of the thin-walls ranges from 36 to 183 (11 mm long [constant], and 0.3 mm to 0.06 mm in thickness). These thin-wall test artifacts were built under three angular orientations, 0° , 60° , and 90° . Further, the parts were examined offline using X-ray computed tomography (XCT). Through the offline XCT data, the build quality of the thin-wall features in terms of its geometric integrity was quantified as a function of the aspect ratio and orientation angle, which helped codify a set of design guidelines for building thin-wall structures with LPBF. The resulting geometric design rules are summarized as follows.

- 1) The orientation angle (θ) of 90° should be avoided while building thin-wall structures.
- 2) The aspect ratio (l/t) of a thin wall should not exceed 73 (11 mm / 0.15 mm).
- 3) The height of a thin wall should not be more than nine times its thickness.

To monitor the quality of the thin-wall, in-process images of the top surface of the bed were acquired during the build process. The online optical images were correlated with the offline quantitative measurements of the thin walls through a deep learning convolutional neural network (CNN). The statistical correlation (Pearson coefficient, ρ) between the offline XCT-measured thin-wall quality, and the CNN predicted measurement ranged from 80% to 98%. Consequently, the impending poor quality of a thin wall was captured from in-process data.

The data for this work was acquired at Pennsylvania State University by Dr. Edward Reutzler and his research group in the Applied Research Laboratory.

Acknowledgements

Firstly, I would like to thank my thesis advisor Dr. Prahalada Rao of the Mechanical and Materials Engineering department at University of Nebraska-Lincoln. Dr. Rao's consistent support, guidance and motivation has been the driving force in completion of this work. His inclination towards attention to detail and perfection has played an anchor role in shaping this thesis. I would also like to thank the thesis committee members; Dr. K.P. Rajurkar and Dr. R. Williams, for their valuable input to improve the quality of this work.

I would like to acknowledge the help and support of Dr. Edward Reutzel, Dr. Hui Yang and Mr. Farhad Imani from the Pennsylvania State University. This thesis would not have been possible without the data provided by Dr. Edward Reutzel and the help provided by Dr. Hui Yang and Mr. Farhad Imani in the preliminary analysis.

I would also like to thank the National Science Foundation (NSF) for supporting this work through grant no. CMMI 1752069 (PI Rao).

Lastly, and most importantly, I would like to thank my parents; Chandrashekhar and Manisha Gaikwad, for their undying support, trust and faith in me. I would also like to thank my elder brother, my role model; Mr. Aditya Gaikwad, for guiding me throughout my life and helping me through difficult times.

Table of Contents

Chapter 1 Introduction	1
1.1 Background and Motivation	1
1.2 Objectives	3
1.3 Organization of the thesis	6
Chapter 2 Literature Review	7
2.1 Design for additive manufacturing (DFAM)	7
2.2 In-situ sensing and monitoring in laser powder bed fusion (LPBF)	12
Chapter 3 Experimental Studies.....	19
3.1 Test-artifact with thin walls	19
3.2 Setup for in-process powder bed imaging	21
Chapter 4 Methodology	24
4.1 Offline Analysis of build quality using layer-wise XCT scanned images..	26
4.2 Online Analysis of in-process powder bed images.....	33
Chapter 5 Results	46
5.1 Geometric design rules for thin-walls based on offline XCT scan images.	46
5.2 Results from in-process powder bed image analysis	50
Chapter 6 Conclusions and future work.....	52
References Cited	54

List of Figures

Figure 1-1: Representation of the laser-based powder fusion process [1].....	1
Figure 1-2: X-Ray computed tomography (XCT) scan of a titanium spinal implant consisting of thin-wall structures.....	2
Figure 1-3: (a) A schematic of various defects that may occur in LPBF of a thin-wall structure. (b) XCT scan of a thin-wall part at 60° orientation angle. The thin walls with aspect ratio of 55 (l/t , 11 mm/ 0.15 mm) and 36 (11 mm/ 0.1 mm) are shown (c1) and (c2) respectively. These images depict the different defects evident in thin-wall structures.....	6
Figure 2-1: (a) Test specimen designed by Kranz et al. to study the effect of part position on the accuracy of the part. (b) Different positions at which the test specimen was placed to study the effect of part position on the part accuracy [24]	11
Figure 2-2: Test specimen drawing adopted from Adam et al. [26]. The test specimen is built in three different orientations, namely, (a) depth of specimen along the X-Y axis, (b) height of the specimen along the Z-axis, and (c) height of the inverted specimen along the Z-axis of the build direction.....	12
Figure 2-3: A summary of the design rules formulated in works described in section 2.1.....	18
Figure 3-1: Computer aided design (CAD) of thin walls in the test part. (a) Top view, (b) front view. (c) 3-D view of the test part along with the re-coater blade.....	20
Figure 3-2: Illustration of the optical DSLR camera and flash lamps used for acquiring in-situ data [35].	21
Figure 3-3: In-process powder bed images captured under different lighting schemes [1]. The different lighting schemes are obtained with the help of flash-lamps which are placed at various locations in the machine, as shown in Figure 3-2.	22
Figure 3-4: In-process optical images of a layer of thin walls being manufactured at different orientation angles in the X-Y plane with respect to the re-coater blade direction, namely, (a) 0°, (b) 60°, (c) 90°.	23

Figure 3-5: Schematic representation of the two different hatch patterns used to build thin walls. (a) Hatch pattern used to build thin walls with aspect ratio (l/t) ranging from 36 to 157, i.e., thickness of 0.07 mm to 0.3 mm (thin wall number 2 to 25). (b) Hatch pattern used to build thin wall number 1 with aspect ratio (l/t) of 183, i.e., thickness of 0.06 mm. 23

Figure 4-1: Outline of the methodology adopted to analyze XCT scan data with the help of CAD data for the thin walls (offline analysis), and in-process powder bed images (online analysis). 25

Figure 4-2: Layer number 18 of thin-wall parts at three different orientations. The top panel shows layer number 18 of thin walls at three orientations, and the bottom panel shows thin wall number 20 ($l/t=44$, thickness=0.25 mm) at three different orientations. The thin wall built at 90° orientation has the worst build quality. 27

Figure 4-3: The extraction of thin walls from XCT scan images. Thin wall images shown in (d) and (e) are used to extract features from thin walls to formulate design rules. 28

Figure 4-4: Thin-wall features extracted from XCT scan images. (a) Thin-wall layer image (I) showing thin-wall discontinuity, and highlighting two parts of the thin-wall illustrating other defects. (b) Binarized image of a thin-wall segment (BS) representing thin-wall thickness, thin-wall edge smoothness, and ideal thin-wall profile. (c) Image of thin-wall segment (IS) depicting thin-wall density. 29

Figure 4-5: A representation of the thin-wall thickness feature. The pixels highlighted in red represent the pixels in the upper and lower edge of the thin wall. 30

Figure 4-6: A representation of the arrangement of the quantifier matrix for a thin-wall 33 at 0° orientation angle. The features extracted from the first XCT scan thin-wall image with a particular aspect ratio and an orientation angle of 0° is represented by $\bar{X}_1^{0^\circ}$. The vector with features extracted from the CAD images of a thin wall with a particular aspect ratio is represented by μ^{TW} 33

Figure 4-7: Schematic representation of image de-noising done by employing image sharpening. This technique uses a filter matrix which convolves around an image. 34

Figure 4-8: Flow-chart of the architecture of the convolutional neural network employed in this thesis to predict Mahalanobis-squared distance.	37
Figure 4-9: Schematic representation of convolution operation.	38
Figure 4-10: Schematic representation of an average pooling operation.	42
Figure 4-11: The schematic representation of the convolutional neural network architecture.	45
Figure 5-1: Mahalanobis-squared distance for different orientations (θ) of different thin walls. (a) Thin wall number 10, with aspect ratio (l/t) of 73, i.e., length $l= 11$ mm and thickness $t= 0.15$ mm. (b) Thin wall number 20, with aspect ratio (l/t) of 44, i.e., length $l= 11$ mm and thickness $t= 0.25$ mm.	47
Figure 5-2: Maximum recommended height to build thin walls of good geometrical integrity with respect to aspect ratio (l/t).	48
Figure 5-3: Maximum build height of thin-walls to get good geometrical integrity, and height at which thin walls collapse, with respect to aspect ratio and orientation angles. .	49
Figure 5-4: Summary and pictorial description of the geometric design rules formulated from this work for thin-wall features built using laser powder bed fusion additive manufacturing process.	50
Figure 5-5: Mahalanobis-squared distance prediction via CNN regression for thin wall number 23 ($l/t= 39$, length= 11 mm, thickness= 0.28 mm) with (a) 0° orientation, (b) 60° orientation and (c) 90° orientation.	51

CHAPTER 1 – INTRODUCTION

1.1 Background and Motivation

This thesis aims to understand the link between part design features (geometry), in-process sensor signatures, and build quality of parts made using the laser powder bed fusion (LPBF) additive manufacturing (AM) process, specifically focusing on thin-wall features. In LPBF (Figure 1-1), a thin layer of powder is raked or rolled across a build plate, and subsequently, this layer of powder is selectively melted using energy supplied by a laser beam [2]. The laser beam is typically focused on the powder bed through an F-theta lens, which maintains a fixed focal length irrespective of the angle of incidence of the laser beam [3]. For most materials processed in LPBF, the power of the laser beam is set in the range of 200 W to 500 W, and the velocity with which it travels ranges from 500 mm/s to 1000 mm/s. Following the selective melting of a layer of powder, the build plate is moved downwards by a distance usually in the range of 50 μm to 100 μm , and another layer is deposited [4]. Thus, the part builds layer-by-layer. In LPBF, the part design, process parameters, thermal phenomena, and resulting part microstructure and mechanical properties are intertwined [5].

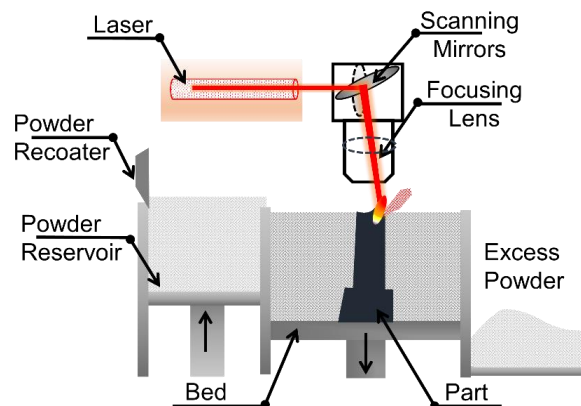


Figure 1-1: Representation of the laser-based powder fusion process [1].

Thin-wall structures are extensively used in industrial applications, wherein there is a need to reduce the weight of a component without losing its structural integrity. Figure 1-2 shows a titanium spinal implant consisting of thin-wall structures. The manufacture of such intricate geometry is difficult with subtractive and formative (conventional) manufacturing processes, and it is made possible through LPBF [6-9]. However, the process anomalies in LPBF, and the inherent geometry of thin-wall structures make these structures highly susceptible to failures, such as, collapse, super-elevation, porosity, poor structural quality etc. [10-12]. In this thesis, an attempt is made to analyze these defects in thin walls, in order to propose quantitative geometric design rules, and an in-situ monitoring system of thin-wall quality.

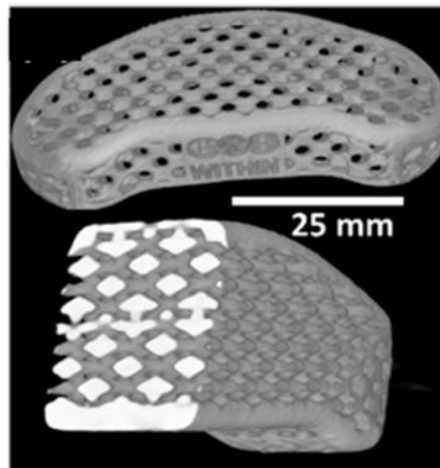


Figure 1-2: X-Ray computed tomography (XCT) scan of a titanium spinal implant consisting of thin-wall structures.

In the context of this work, representative build defects observed in a test artifact with thin-wall features are shown in Figure 1-3. The geometric integrity of the thin wall can be affected by the restricted heat flux due to its smaller cross-sectional area. The restricted heat flux leads to sharp thermal gradients, which in turn may cause cracking and warping (distortion) defects [13, 14]. Another common reason for the frequent failure of

thin-walls is the interaction of thermal and mechanical factors; the geometric distortion of the thin-wall due to the thermal gradients causes the part to protrude out of the powder bed, a phenomenon called super-elevation, which leads to contact of the part with the re-coater [15, 16]. The contact of the part with the re-coater is liable to damage the re-coater (re-coater jam or crash), and the thin-wall features may fail as they are ill-disposed to resist the axial force exerted by the re-coater. Given these reasons, there is a compelling need to provide design rules for hard-to-build features, such as thin walls and overhang geometries, so that extensive process optimization is precluded. Within the same context, it is critical to detect imminent build failures and then implement opportunistic corrective actions in a hybrid AM machine [17, 18].

1.2 Objectives

In the context of the aforementioned scientific rationale concerning design rules and process monitoring in AM, the objectives of this work are as follows:

- 1) Formulate geometric design rules for the manufacture of high aspect ratio (length-to-thickness ratio, l/t) thin-wall parts made using the LPBF process. These design rules take the following form: given a build orientation and height of a thin-wall feature, what should be its thickness. Alternatively stated, given an aspect ratio of a thin wall, what should be the maximum allowable build height, and corresponding build orientation.
- 2) Detect the onset of build failures in thin-wall parts using data from in-process sensors built into the machine.

To achieve the first objective, we designed a test artifact having thin-wall features with an aspect ratio (length-thickness ratio, l/t) ranging from 36 to 183; these corresponded to 11 mm length and 0.3 mm thickness to 11 mm length and 0.06 mm thickness. The details of the test artifact are discussed in Chapter 3; a schematic of the thin wall shown in Figure 3-1. Three such test artifacts were built, each differing in its angular orientation (θ) to the re-coater. Subsequently, we examined each of the thin-wall builds using X-ray computed tomography (XCT) (e.g. Figure 1-3(b)). The build quality of the thin wall was quantified using features extracted from layer-wise XCT slices with the help of image processing algorithms. These features were tracked across layers and were thereafter used as derived features of thin walls. Geometric design rules for thin-wall features were proposed based on these empirical quantitative measures.

To address the second objective, we developed an in-process optical imaging setup that took a picture of the surface of the powder bed after each layer was deposited. These images were further analyzed using a convolutional neural network (CNN), which is a multi-layered neural network which is used to detect low and high level pattern/features, such as line, curve, hand, text, etc., from an image. The feature detection process in CNN is based on the learning process that used in a feedforward artificial neural network (ANN). These networks have three primary layers, namely, input layer, hidden layer and output layer. The input layer forwards the data to the hidden layers that has non-linear activation functions. The output layer computes the error between the predicted outcome and the observed outcome. This error is sent back into the network to make parametric changes in the network in order to reduce the error. This technique of training a network is called backpropagation. Once the network is trained, i.e., lowest possible error is achieved for a

given configuration of the network, it is tested to calculate the accuracy. In this work, we used the in-process powder bed images to train the CNN to predict the build quality features extracted from XCT images from the first objective. As a consequence, the part quality, in terms of its geometric integrity could be tracked using the in-process data to pre-empt failure.

The novel contribution of this work is that it makes the following key links in the laser powder bed fusion (LPBF) process chain in the specific context of thin-wall geometry parts.

Part geometry + orientation → Process signatures → Part quality

First, it provides new knowledge linking the part geometry and orientation to the build quality in laser powder bed fusion (LPBF). Specifically, it demarcates the effect of orientation angle and aspect ratio (length-to-thickness ratio) on manufacturability of thin-wall parts using LPBF. This knowledge is valuable for practitioners, as it provides them with a design guideline for building thin-wall parts that are extensively used in engineering components, such as heat exchangers and lattice-like shapes.

Second, this work links in-process signatures with the part quality. To explain further, the process signatures in this work relate to the in-situ optical images of the powder bed. A novel deep learning convolutional network is used to identify patterns of impending failures in the part from images of the powder bed.

This work thus has two key outcomes:

- (1) design guidelines for producing thin-wall parts in terms of the maximum height achievable given an aspect ratio, and recommendations for orientations of a thin wall orientation; and
- (2) in-situ monitoring of thin-wall quality using layer-wise optical imaging.

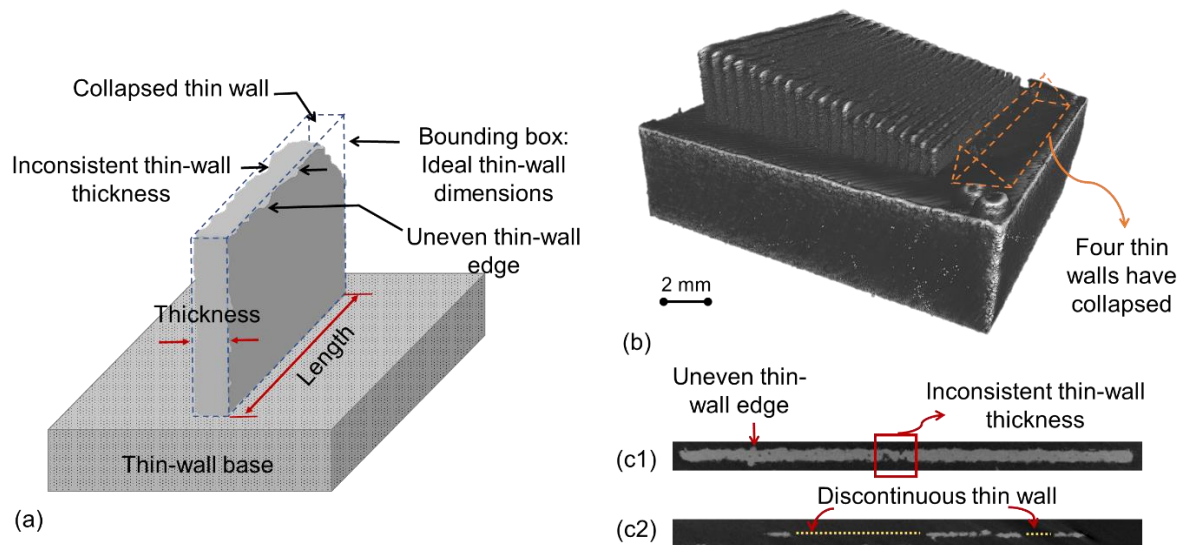


Figure 1-3: (a) A schematic of various defects that may occur in LPBF of a thin-wall structure. (b) XCT scan of a thin-wall part at 60° orientation angle. The thin walls with aspect ratio of 55 (l/t , 11 mm/ 0.15 mm) and 36 (11 mm/ 0.1 mm) are shown (c1) and (c2) respectively. These images depict the different defects evident in thin-wall structures.

1.3 Organization of the thesis

The organization of this thesis is as follows: A brief summary of the relevant literature from the design for AM is provided in Chapter 2. This is followed by the description of the experimental procedure in Chapter 3, including a summary of the thin-wall test artifact, and a procedure for data acquisition. Chapter 4 describes the methodology used for quantification of thin-wall build quality from XCT scan data, and the detailed analysis of the in-process powder bed images using a deep learning convolutional neural network (CNN). The results from this work are discussed in Chapter 5, in which the geometric design rules derived from the analysis of XCT scan slices are put forth, and the fidelity of the CNN in predicting the quality of the thin wall is quantified. Finally, the conclusions of this work, and further research directions are summarized in Chapter 6.

CHAPTER 2 – LITERATURE REVIEW

2.1 Design for additive manufacturing (DFAM)

The powder bed fusion (PBF) additive manufacturing (AM) processes, despite their revolutionary potential, intrinsically have shortcomings, such as material constraints, surface finish, part accuracy and repeatability, which have impeded their use in a production environment [19]. Furthermore, parts that are additively manufactured have particular distinguishing characteristics, such as intricate geometries, custom part design, low production volume, and complex material compositions [20]. One of the main bottlenecks in AM is the absence of design guidelines that can be used as rules-of-thumb by practitioners to avoid poor quality parts [21]. It is therefore essential to propose design guidelines for AM. According to Rosen, the design for additive manufacturing (DFAM) is defined as, “*Maximizing product performance through the synthesis of shapes, sizes, hierarchical structures, and material compositions, subject to the capabilities of AM technologies* [20].”

The conventional design for manufacturing (DFM) rules do not apply for AM parts as they are manufactured layer-by-layer, and are bottom-up processes, unlike the conventional methods, such as machining, which are top-down. Hence, the unique layer-by-layer nature of AM mandates a different approach to part design compared to traditional manufacturing processes. Ponche et al. have introduced a general methodology for DFAM in which they primarily focus on the orientation of the part, its geometry which is established using topological optimization, and the process conditions, such as the laser parameters, that need to be employed for the part [22]. According to Ponche et al., part orientation refers to positioning the functional surfaces of a part being designed in such a

way that it leads to the best surface finish and accuracy. The part geometry can be potentially designed with the help of topological optimization, i.e., for a given design space, set of loads, set of constraints and boundary, the material layout is optimized to achieve high performance of the system [23]. Similarly, Kranz et al. have recommended design guidelines for laser additive manufacturing (LAM) by analyzing the effect of part orientation, size, and position on the dimensional accuracy and surface finish of lightweight parts, such as, thin-walls, bars etc. [24]. The effect on surface quality of a part was studied by manufacturing parts with upward-and-downward-facing surfaces which were built at various orientation angles with reference to the build platform. Kranz et al. observed that parts with the smallest orientation angle had the lowest (best) surface roughness.

To study the effect of part position in the powder bed on part accuracy, they designed test parts, which included a rectangular structure, a cylindrical structure, and a thin-wall structure (Figure 2-1 (a)), and placed this test part in five different locations on the powder bed namely, middle, upper right, upper left, lower right, and lower left (Figure 2-1 (b)). It was concluded that the part position had no discernable effect on the accuracy of the test geometry for this particular experimental setup. Further, to study the effect of orientation and size on part accuracy, parts with three different cross-sections, such as, elliptical, cylindrical, and rectangular were chosen, and the aspect ratios (length-to-thickness ratio, l/t) of each part were varied. For thin-wall structures (rectangular cross-section), it was observed that to obtain good quality, the thickness should be greater than 0.4 mm, the orientation angle with reference to the build platform should be 90° , and the orientation angle with reference to the re-coater device should be 45° (Figure 2-3). The study on bore

holes (cylindrical cross-section) showed that the highest part accuracy is obtained when it was built orthogonal to the build platform.

A detailed study on design rules was done by Daniel Thomas in his doctoral dissertation [25]. The author studied fundamental geometries, such as overhang features, which could then be used for designing complex geometries. Through study of a simple cuboidal structure, the author observed that orientation of the part (with reference to the build surface) played an important role in the surface quality of the part. It was observed that support structures were required to avert build failure when surfaces were built under an orientation angle of 45° to the build platform. The optimum orientation angle to the build surface was seen to be 90° to the build platform (Figure 2-3). The author suggested that the *up-facing* surfaces had poor surface quality under the 45° orientation angle, but the surface quality abruptly improved at 0° to the build platform. To build geometries such as overhangs without support structures, the author suggested using features which eschew the need for support structures; namely, chamfers, and convex and concave radii. Thomas reported that chamfers can be built with an orientation angle (with reference to the build plate) of more than 45° (Figure 2-3). The convex and concave radii need to be built at varying bottom and top tangent angles of the radii to avoid support structures, and these angles can be found in a tabulated format in the author's dissertation [25]. Further, to prevent surface merging while building parts such as, channels, slots, keyways etc., it is necessary to have a minimum gap between features which was found to be 0.3 mm in this research (Figure 2-3). Additionally, the author's research conforms with the results obtained by Kranz *et al.*, that the minimum thickness of the thin wall should be 0.4 mm [24, 25]. Subsequently, holes were also studied by Kranz et al. It was recommended that

the minimum hole size should be 0.7 mm diameter when they are built parallel (self-supporting) to the build plate, and 1 mm when built perpendicular to the build plate.

In a study by Adam et al., design rules for two types of structures, namely, *element transitions*, and *aggregated structures*, were formulated [26]. According to the authors, the combination of basic elements (e.g., cuboidal structures) are called element transitions (e.g., joints), and the arrangement of these element transitions along with multiple basic elements are called aggregated structures (e.g., overhangs). To study the effect of varying thickness and orientation on element transitions, a Y- shaped test specimen was designed (Figure 2-2). This test specimen was built in three different orientations as seen in Figure 2-2, and the thickness (T_1, T_2, T_3) of the three elements was varied between 2 mm and 5 mm, namely, $T_1 = 2$ mm, $T_2 = 5$ mm, $T_3 = 5$ mm. the authors found no evidence that the aforementioned orientations affected the part quality. However, they concluded that thicknesses should be chosen so that the cross-sectional areas of element transitions in the build plane would remain the same size, or would reduce to avoid surface defects, i.e., the cross-sectional areas of elements T_1 and T_2 should remain same or be less in comparison to that of T_3 (Figure 2-3). Further, they studied the effect of edge morphology on part quality. It was concluded that to avoid defects, parts with sharp outer edges should be avoided, and similarly, parts should not have sharp inner edges for ease of removal of support structures and residual powder. Finally, structures which have non-bonded elements, should have the following minimum gap (H_G) values for different AM process: laser sintering (SLS) ($H_G \geq 0.6$ mm), laser melting (LPBF) ($H_G \geq 0.2$ mm), and fused filament fabrication (FDM) ($H_G \geq 0.4$ mm) (Figure 2-3). In the case of aggregated structures (namely, overhang), to ensure a robust manufacturability the authors suggested

that the length of the overhang should be as follows: laser melting ($L_{OH} \leq 2.0$ mm), and fused filament fabrication ($L_{OH} \leq 1.8$ mm) .

A summary of the design rules established from the above discussed works is given in Figure 2-3. Most of these pioneering works formulated design rules for AM based on measurements made with rudimentary instruments, such as calipers, which do not capture the geometric and build integrity in a more detailed manner. In this thesis, we introduce design rules by analyzing data from X-ray computed tomography (XCT) scan, and layer-wise in-process images of the test specimen.

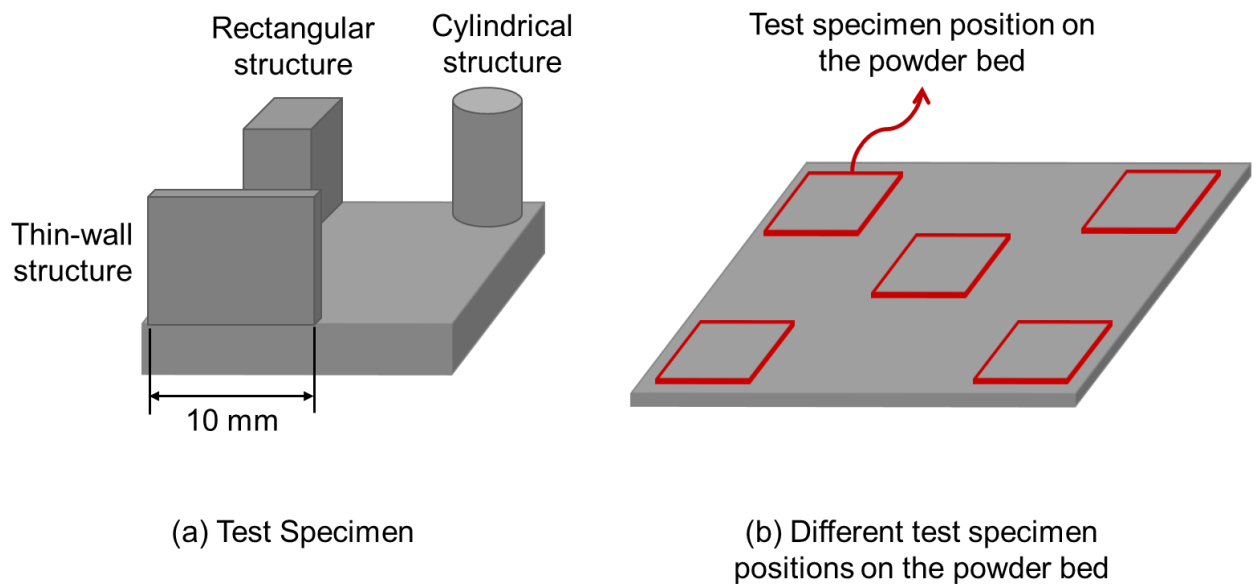


Figure 2-1: (a) Test specimen designed by Kranz et al. to study the effect of part position on the accuracy of the part. (b) Different positions at which the test specimen was placed to study the effect of part position on the part accuracy [24]

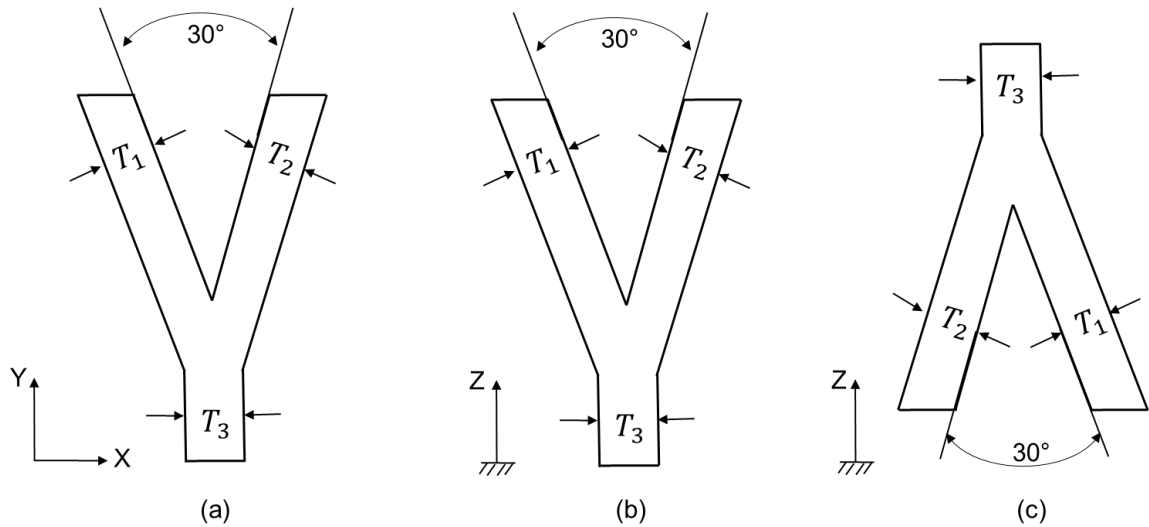


Figure 2-2: Test specimen drawing adopted from Adam et al. [26]. The test specimen is built in three different orientations, namely, (a) depth of specimen along the X-Y axis, (b) height of the specimen along the Z-axis, and (c) height of the inverted specimen along the Z-axis of the build direction.

2.2 In-situ sensing and monitoring in laser powder bed fusion (LPBF)

Additive manufacturing (AM) processes have seen an exponential growth in industrial applications because of their ability to build lightweight parts with complex geometries. Owing to these capabilities, there is a demand for AM parts in the medical and aerospace industry. In these industries, it is mandatory that the parts should have high quality, and repeatability [10]. Despite their revolutionary capabilities, practitioners have found that AM processes are not sufficiently reliable and repeatable in production to replace their conventional manufacturing counterparts, as they result in formation of a high number of defects [4, 27-29]. To tackle this hurdle, it is necessary to implement in-situ sensing, monitoring, and feedback control techniques in AM processes. The use of in-process sensing and monitoring will facilitate understanding the effect of process conditions on defect formation, and thus the product quality. Upon recognizing the incipient formation

of flaws, a feedback control system can be designed to correct these defects in-situ (inside the machine), and thus reduce the scrap rate.

Nassar et al., have developed a sensing system for defect detection during AM of Ti-6Al-4V, wherein they employed optical emission spectroscopy to determine the occurrence of lack-of-fusion defects by correlating them with the line-to-continuum ratio of the spectral atomic line emissions[30]. The test specimen used in this study was a rectangular block which has an increasing hatch spacing from one end to the other; viz., 0.914 mm to 1.829 mm with an increment of 0.229 mm after every 10 mm along the length. It was observed that the line emissions ranging from 625 nm to 395 nm were intense in regions with defects for ASTM grade 5 titanium (Ti-6Al-4V).

In another work by Nassar et al., they devised an in-situ sensing and monitoring technique, wherein they used a supervised machine learning approach to detect defects from in-situ optical images [31]. The authors proposed a methodology to predict defects, such as cracks, porosity, incomplete fusion etc., by first extracting them from the X-ray computed tomography (XCT) scan of the test specimen. These defect and nominal condition voxel locations were then mapped on to the layer-wise optical images; and then a binary classifier, called support vector machine (SVM), was used to predict the flawed and nominal locations in the optical images. The authors demonstrated that they achieved an accuracy of over 80% while testing this classifier to predict defect and nominal condition locations.

Abdelrahman et al., in a recent work, developed an in-situ flaw detection system that used layer-wise optical images of a powder bed fusion process [32]. This system captured images of the powder bed prior to and post re-coat of the layer, and each of these images

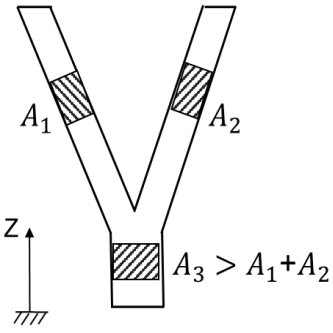
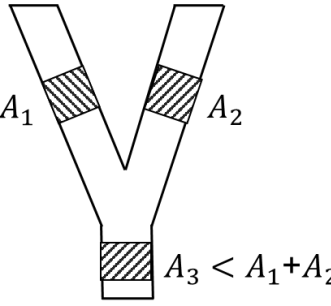
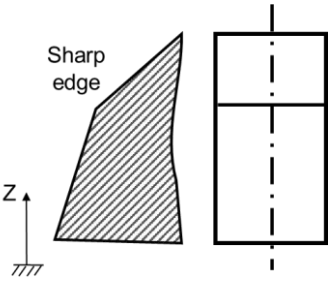
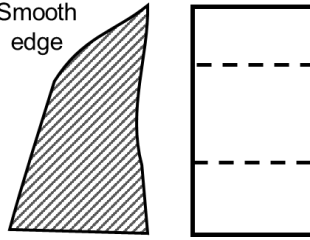
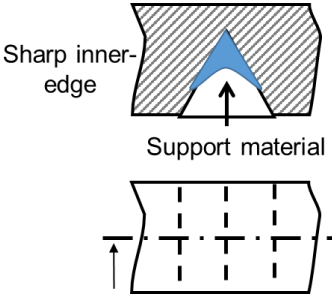
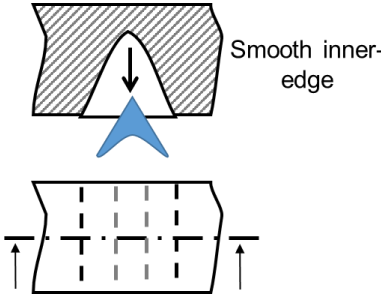
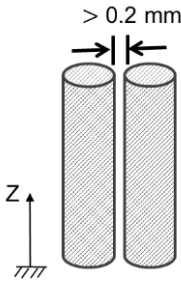
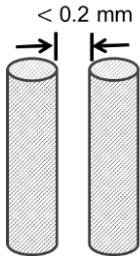
is captured in five different lighting schemes, so that the surface perturbations are magnified, and the defect detection is accurate. The test specimen had intentional defects in it, and these defects were detected by correlating the multiple lighting condition images of the multiple layers with a high true positive rate.

Montazeri and Rao, have developed a heterogeneous sensor-based process monitoring system, to detect defect formation in the laser powder bed fusion process [2]. In this study, the meltpool characteristics were monitored with help of a heterogeneous sensor array consisting of a thermal camera and photodetector, which monitored the thermal aspects of the meltpool, and a high speed camera which captured the meltpool shape and surrounding spatter pattern. The test specimen used in this work had a distinct overhang, and the authors tried to differentiate between the meltpool behavior while processing the overhang and non-overhang part. This was done by representing the signals from the three sensors as a multi-dimensional data set, and then using a spectral graph theoretic approach to analyze the data, and thus differentiating between build locations.

Using the spectral graph theoretic approach, Montazeri et al., tried to detect material contamination in powder bed fusion with the help of photodetector signals [33]. To achieve this goal, the powder bed was intentionally contaminated, and then the hatch-by-hatch photodetector signals were analyzed to detect the contamination. Further, Imani et al., used a spectral graph theoretic and multi-fractal approach to monitor layer-wise in-situ process conditions with the help of optical images [1]. They predicted the process condition in which the part was being built with a statistical fidelity of over 80%. This was accomplished by gathering spectral graph theoretic, and multi-fractal features from the layer-wise powder bed images of test specimens being printed at various printing

conditions. A feedforward neural network was trained on the basis of these features to predict the build condition.

Craeghs et al., have demonstrated a novel way of detecting defects such as deformation resulting from thermal stresses, and overheated overhang structures, by mapping the meltpool in terms of space and not time [34]. The meltpool radiation was split into two signal groups, namely, the infrared region, and the visible light region. The infrared region captured by the photodiode, translated the information of the meltpool temperature in the form of pixel intensity, and the location of the meltpool was monitored by the optical camera. These data sets from the two sensors were then used to create a layer-wise meltpool map.

Author(s)	Description	Unsuitable	Suitable
Adam et al. [26]	The thickness of element transitions' (explained in section 2.1) should be such that the cross-sectional area in the building plane remains constant or reduces.		
	To obtain good outer edge morphology, smooth edges should be used instead of sharp edges.		
	To remove support structures with ease, inner edges should be rounded.		
	Minimum gap between two consecutive features should be more than 0.2 mm.		

	<p>Surfaces should be built vertical, i.e. orientation angle of 90° to the build platform to get good surface finish.</p>		
<p>Daniel Thomas [25]</p>	<p>Thin-wall structures should have thickness greater than 0.4 mm</p>		
	<p>According to Thomas, the gap between consecutive features should be more than 0.3 mm.</p>		
	<p>To build overhang geometries chamfers above the orientation angle of 45° with respect to the build platform can be used as support structures.</p>		

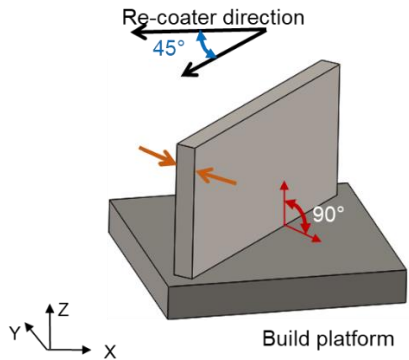
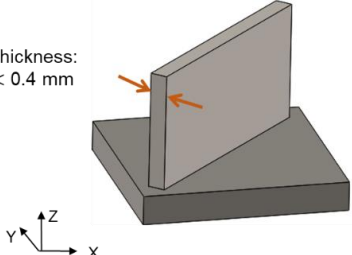
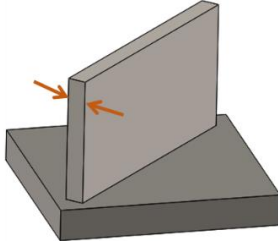
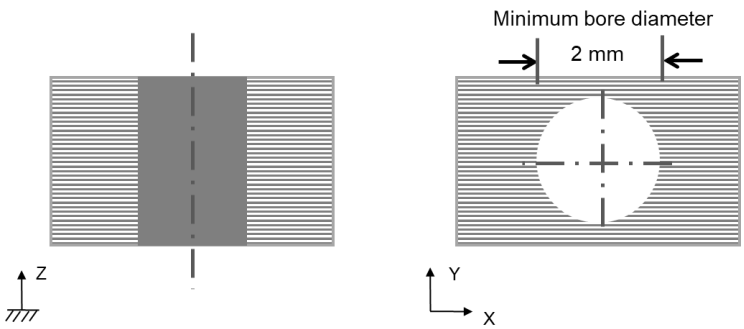
	<p>Thin-wall structures should be built at an orientation angle of 90° with reference to the build platform, and 45° with reference to the re-coater blade direction to get good quality build.</p>	 <p>Re-coater direction 45° Build platform 90° x y z</p>	
<p>Kranz et al. [24]</p>	<p>Similar to Daniel Thomas, Kranz et al. suggest that the thin-wall thickness should be more than 0.4 mm.</p>	<p>Thickness: < 0.4 mm</p>  <p>x y z</p>	<p>Thickness: > 0.4 mm</p>  <p>x y z</p>
	<p>Through bore holes should be preferred over blind holes.</p> <p>The bore diameter should exceed 2 mm for well-defined holes.</p>	 <p>Minimum bore diameter 2 mm z y x</p>	

Figure 2-3: A summary of the design rules formulated in works described in section 2.1.

CHAPTER 3 – EXPERIMENTAL STUDIES

The data for this work was acquired at Pennsylvania State University by Dr. Edward Reutzel and his research group in the Applied Research Laboratory. The experiments described in this chapter were conducted on a sensor integrated EOS Direct Metal Laser Sintering (DMLS) Model M280, Laser Powder Bed Fusion Platform at the Center for Innovative Materials Processing Through Direct Digital Deposition. The experimental portion of this work was supported by the Air Force Research Laboratory through America makes under Agreement No. FA8650-12-2-7230. This work is supported in part by the National Science Foundation (NSF) Center for e-Design (Lockheed Martin) at Pennsylvania State University.

3.1 Test-artifact with thin walls

For building the titanium alloy Ti-6Al-4V thin-wall test artifacts the following process parameters were used: laser power, $P = 340$ W; layer thickness, $T = 0.060$ mm; hatch spacing, $H = 0.12$ mm; and laser velocity, $V = 1250$ mm/s, resulting in the volumetric energy density $E_V = \frac{P}{H \times V \times T} = 37.8$ J/mm³. The parts were made using spherical ASTM B348 Grade 23 Ti-6Al-4V powder with a size distribution of 14 μ m - 45 μ m from LPW Technology, Inc. Parts with the geometry exemplified in Figure 3-1 were built in three angular orientations to the re-coater blade with the dimensions of 15 mm \times 15 mm \times 5.5 mm. Each part included 25 thin-wall features whose thicknesses ranged from 0.06 mm to 0.3 mm, while the corresponding height increased from 0.6 mm to 3 mm. The length of each thin wall was 11 mm, and they were built vertically upwards with a 60 μ m layer thickness. The entire part was built in around 90 layers [35].

In this work, two hatch patterns were used to build thin-wall structures as shown in Figure 3-5. The hatch pattern used to build thin-walls with an aspect ratio (l/t) ranging from 36 to 157, i.e., thickness of 0.07 mm to 0.3 mm (thin-wall number 2 to 25) is shown in Figure 3-5 (a). This hatch pattern had an outer contour, inner contour, and hatches at the

same angle inside the inner contour. The hatch pattern used to build thin-wall number 1 with aspect ratio (l/t) of 183, i.e., thickness of 0.06 mm is shown in Figure 3-5 (b). This thin wall is built with an outer contour, hatches at the same angle, but without an inner contour.

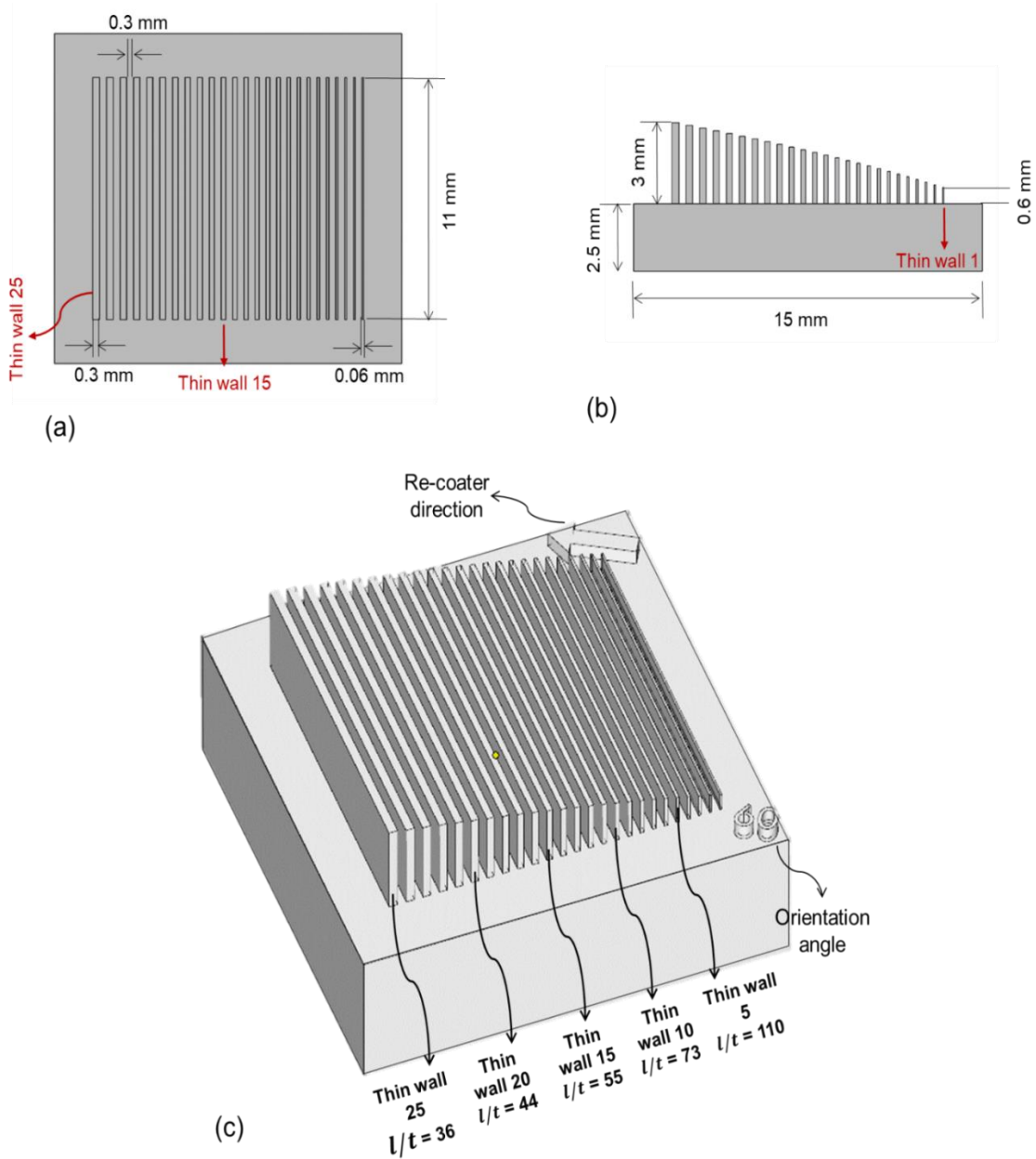


Figure 3-1: Computer aided design (CAD) of thin walls in the test part. (a) Top view, (b) front view. (c) 3-D view of the test part along with the re-coater blade.

3.2 Setup for in-process powder bed imaging

The in-process sensor data was acquired with the setup shown in Figure 3-2. The layer-wise images of the powder bed were captured using a digital single-lens reflex camera (DSLR, Nikon D800E) with an effective resolution of 36.3 megapixels which was mounted in a custom made enclosure inside the machine [32]. The flash lamps were located at three different locations in the machine (EOS M280) as shown in Figure 3-2, and they were used to capture images of the powder bed at every layer in five distinct lighting conditions (Figure 3-2). These images were obtained after the laser scan and after the re-coating, and to capture images at these particular instances during the build, a proximity sensor was employed in the machine. This proximity sensor tracked the motion of the re-coated blade, and accordingly, the images were captured. For this work, we analyzed the images post laser scan with the lighting condition as shown in (Figure 3-3 (a)). The sample data acquired from the apparatus is shown in Figure 3-4.

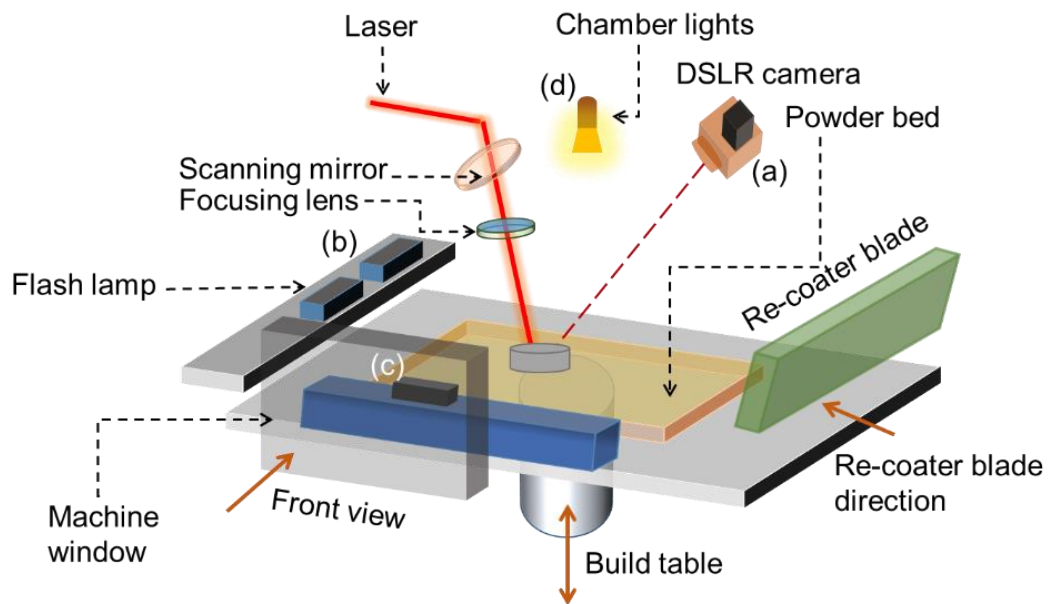


Figure 3-2: Illustration of the optical DSLR camera and flash lamps used for acquiring in-situ data [1].

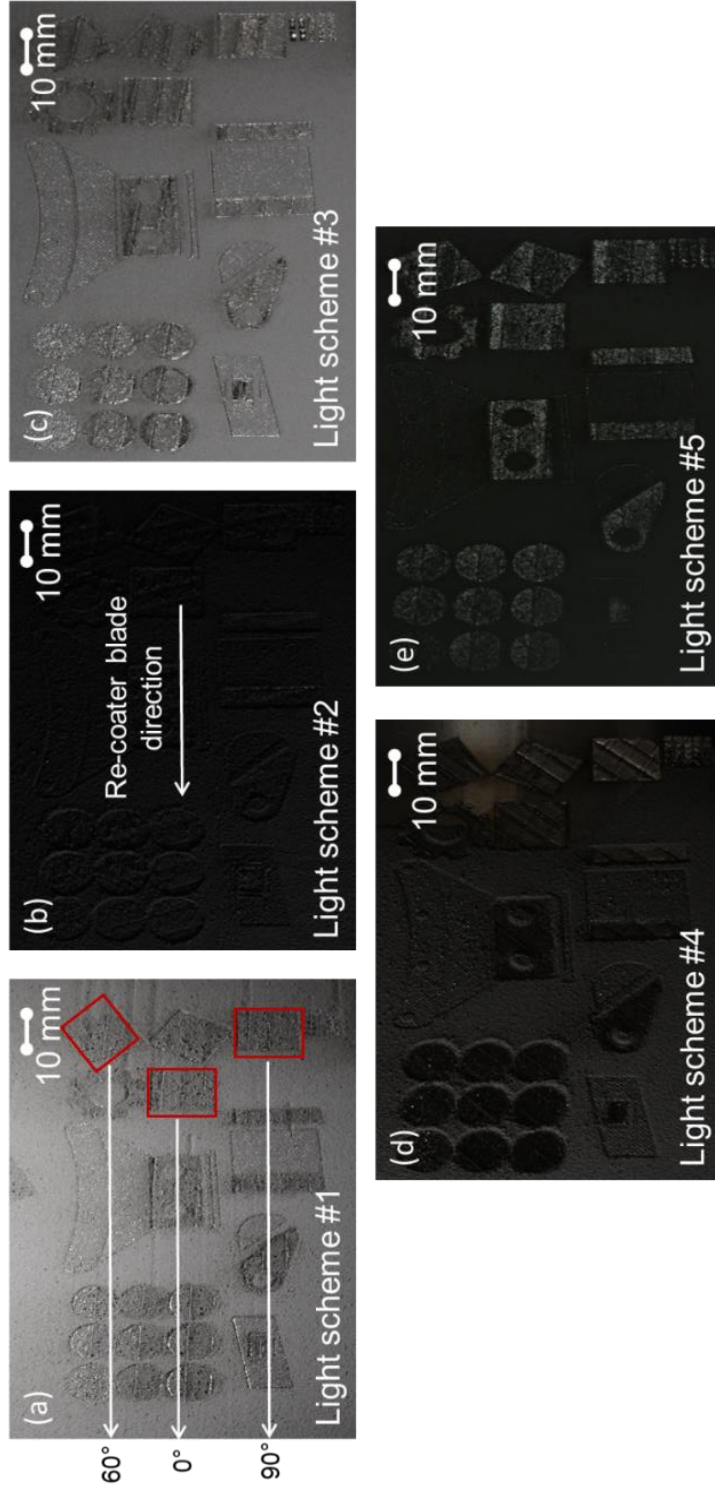


Figure 3-3: In-process powder bed images captured under different lighting schemes [1]. The different lighting schemes are obtained with the help of flash-lamps which are placed at various locations in the machine, as shown in Figure 3-2.

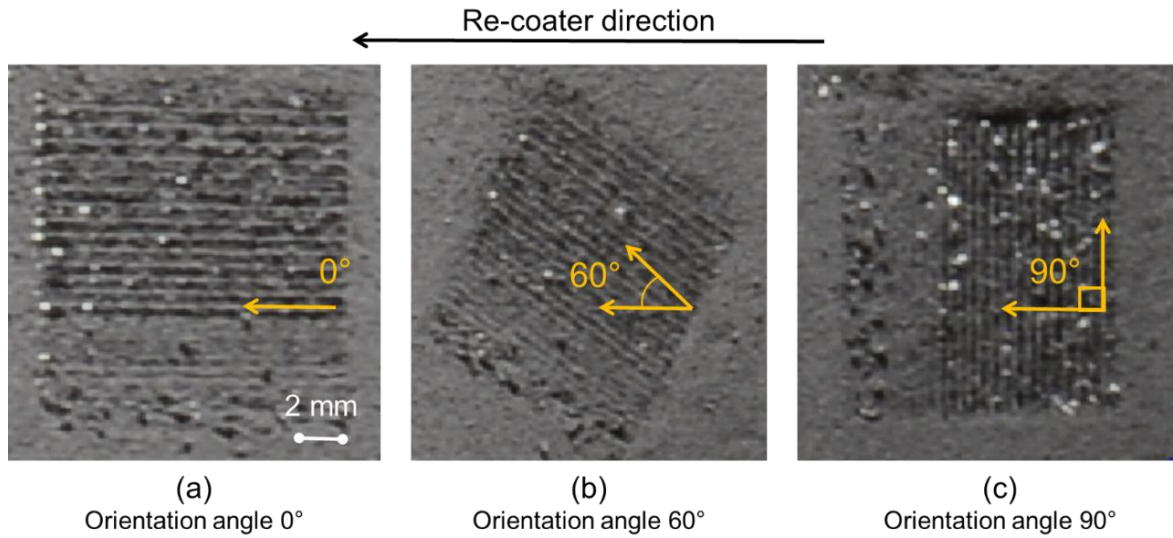


Figure 3-4: In-process optical images of a layer of thin walls being manufactured at different orientation angles in the X-Y plane with respect to the re-coater blade direction, namely, (a) 0°, (b) 60°, (c) 90°.

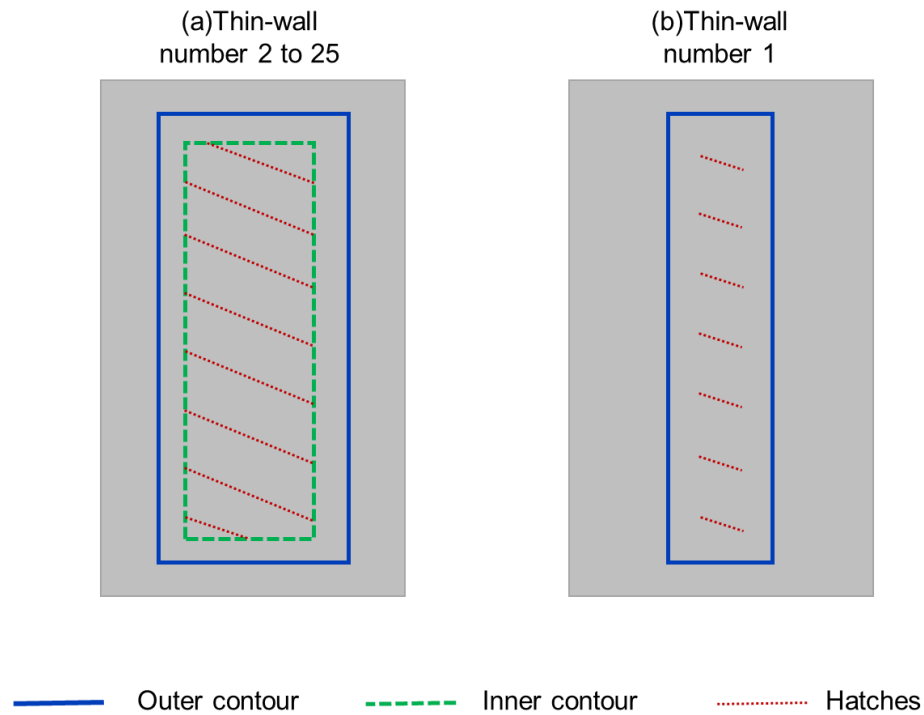


Figure 3-5: Schematic representation of the two different hatch patterns used to build thin walls. (a) Hatch pattern used to build thin walls with aspect ratio (l/t) ranging from 36 to 157, i.e., thickness of 0.07 mm to 0.3 mm (thin wall number 2 to 25). (b) Hatch pattern used to build thin wall number 1 with aspect ratio (l/t) of 183, i.e., thickness of 0.06 mm.

CHAPTER 4 – METHODOLOGY

This chapter is stratified into two sub-sections, wherein section 4.1, discusses the methodology applied to the offline XCT scan image data, and section 4.2, describes the convolutional neural network used to analyze the layer-wise in-situ powder bed images. The research approach is schematically reported in Figure 4-1.

Specifically, section. 4.1 has two phases, the first involves offline analysis of the XCT scan images of the thin-wall geometry (as seen in Figure 4-1), wherein certain quality-related features are extracted from the XCT scan images. These features were then combined in the form of the Mahalanobis-squared distance which was used as a surrogate measure for tracking the build quality of the thin-wall. The next phase was to predict the thin-wall quality from online in-process images. A convolutional neural network (CNN) was used for this purpose, wherein the network was trained to predict the Mahalanobis-squared distance given in-process images of thin-wall boundaries. This neural network known as deep learning convolutional neural network because of the use of convolutional filters on different scales, which learn the aspects of the image from coarse to smooth levels. The modalities of the neural network are discussed in detail in section 4.2.

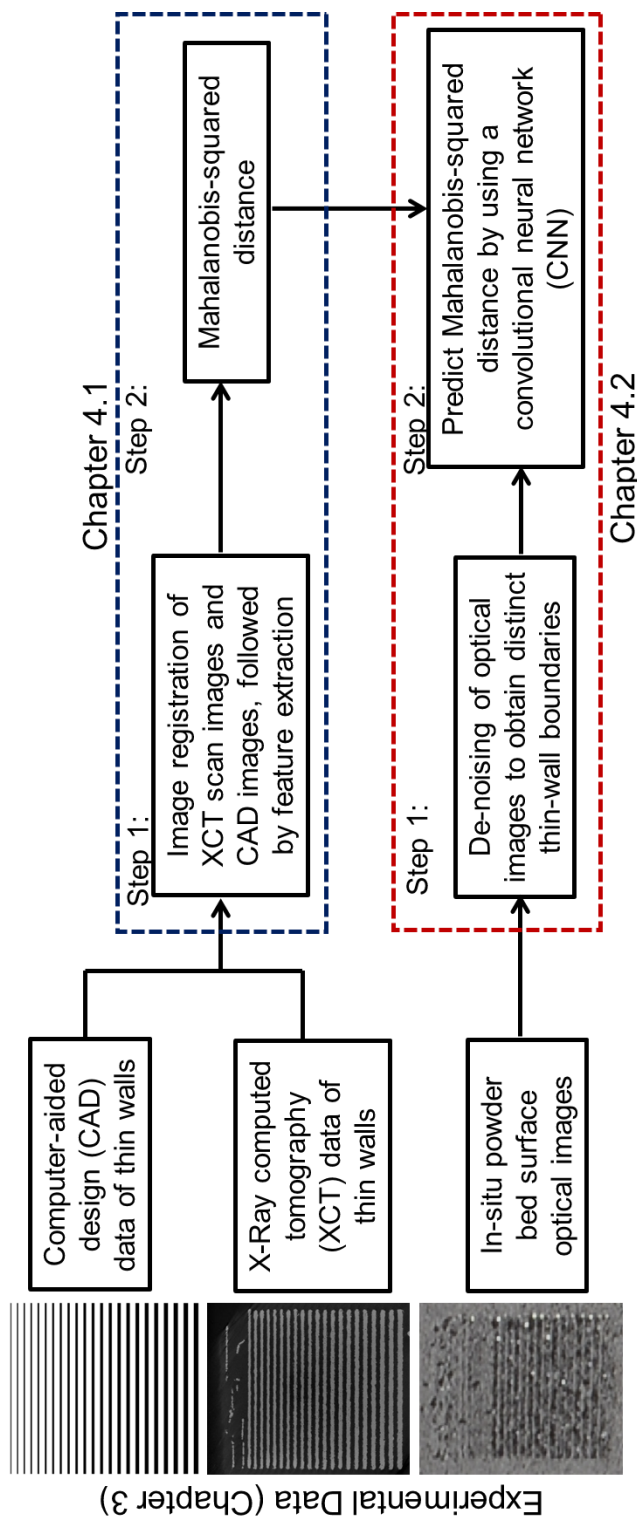


Figure 4-1: Outline of the methodology adopted to analyze XCT scan data with the help of CAD data for the thin-walls (offline analysis), and in-process powder bed images (online analysis).

4.1 Offline Analysis of build quality using layer-wise XCT scanned images

Firstly, the XCT scan of each test artifact is visually (qualitatively) examined layer-by-layer. The following inferences are rendered based on these visual observations. Figure 4-2 shows the example of layer number 18 under the three different angular orientations.

- Thin walls with thickness less than 0.1 mm, i.e., aspect ratio (l/t , length-thickness ratio) greater than 183, cannot be built irrespective of their orientation. The cause of this failure appears to be the overly thin cross-section of the thin-wall, which are too weak to resist the lateral force exerted by the re-coater.
- From the visual inspection of the zoomed in portion of a thin-wall with aspect ratio $l/t= 44$ (Figure 4-2 (b1), (b2), and (b3)) it is evident that the parts printed at orientation angle of 90° generally have poor construct quality as compared to those printed in the other two orientation angles. The probable reason is that in the thin walls built at 0° and 60° orientation angle (θ) the resistance offered to the flow of the powder is less than that at 90° .

These observations were further examined and confirmed by analyzing the sliced images of the fin pad XCT scans.

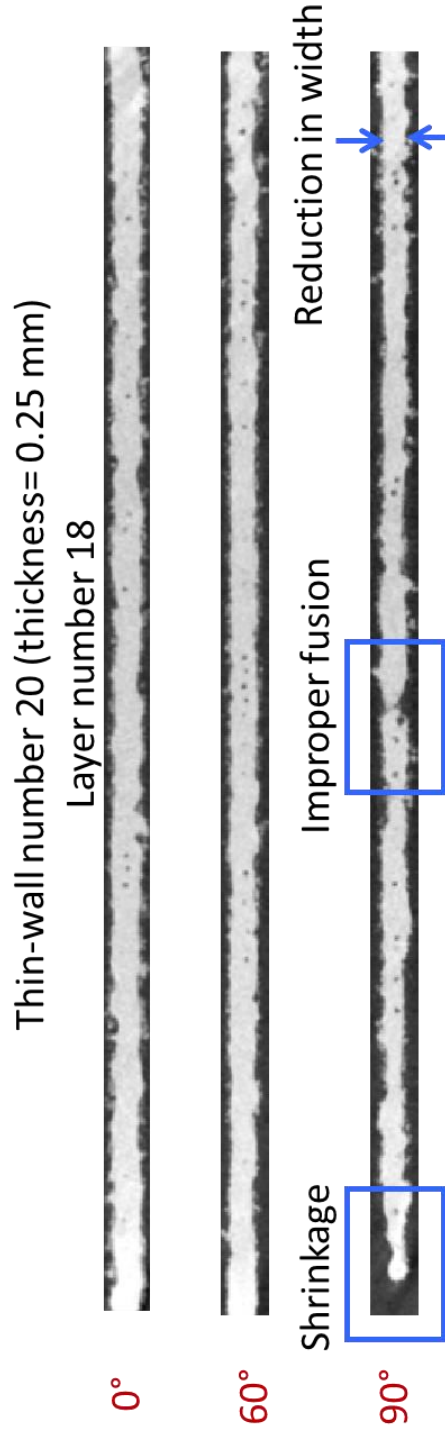
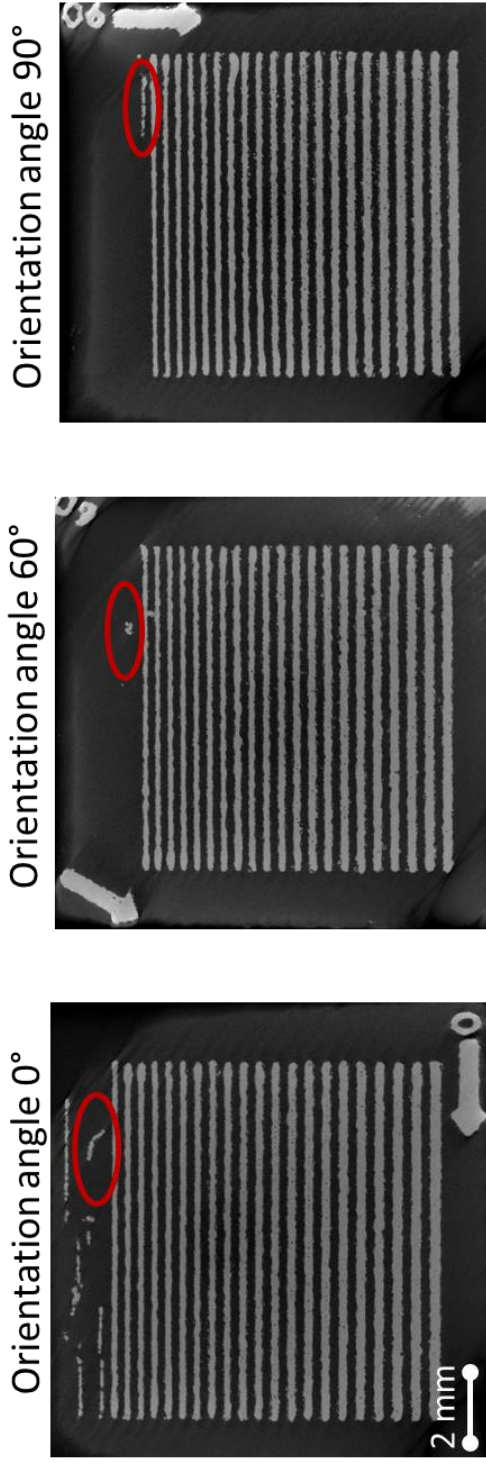


Figure 4-2: Layer number 18 of thin-wall parts at three different orientations. The top panel shows layer number 18 of thin walls at three orientations, and the bottom panel shows thin-wall number 20 ($l/t=44$, thickness=0.25 mm) at three different orientations. The thin wall built at 90° orientation has the worst build quality.

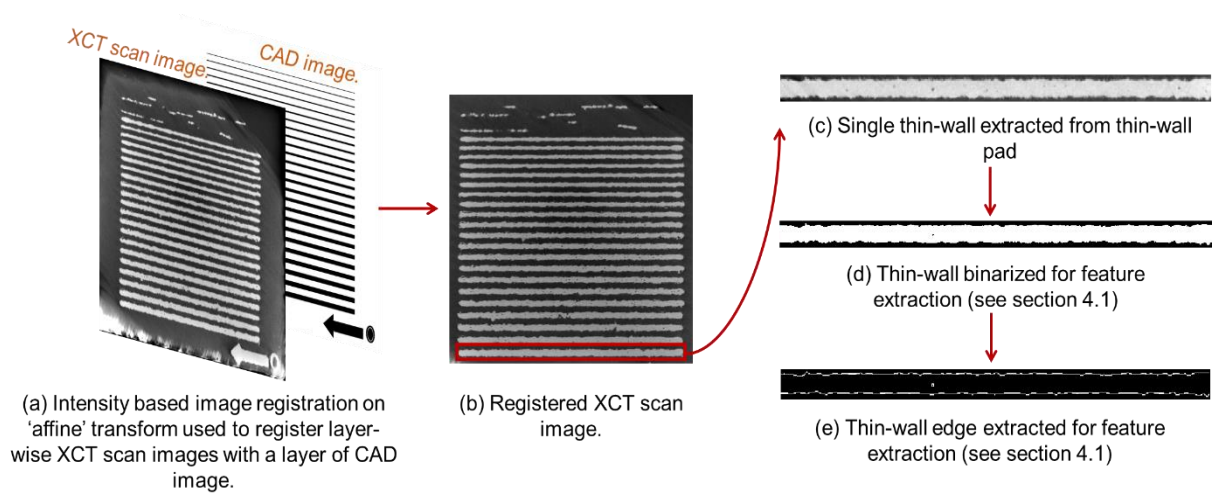


Figure 4-3: The extraction of thin-walls from XCT scan images. Thin-wall images shown in (d) and (e) are used to extract features from thin walls to formulate design rules.

At the outset, the XCT scan for each thin-wall part was sliced with a layer thickness of 10 μm , resulting in 300 images of each part. Subsequently, the CAD file for each test artifact was also sliced with an identical resolution of 10 μm to register the CAD and XCT scan of layer-wise images.

Next, an intensity-based image registration approach was used to perform affine transformation and align the XCT scan image to the corresponding CAD slice. Further, individual thin walls were extracted from the registered images, and each thin-wall was further processed as depicted in Figure 4-3, to extract quantitative features as described shortly. The advantage of using these quantifiers is that they are based on two-dimensional image-based measurements, and involve simple matrix algebra, thus significantly reducing the computational burden involved for feature extraction.

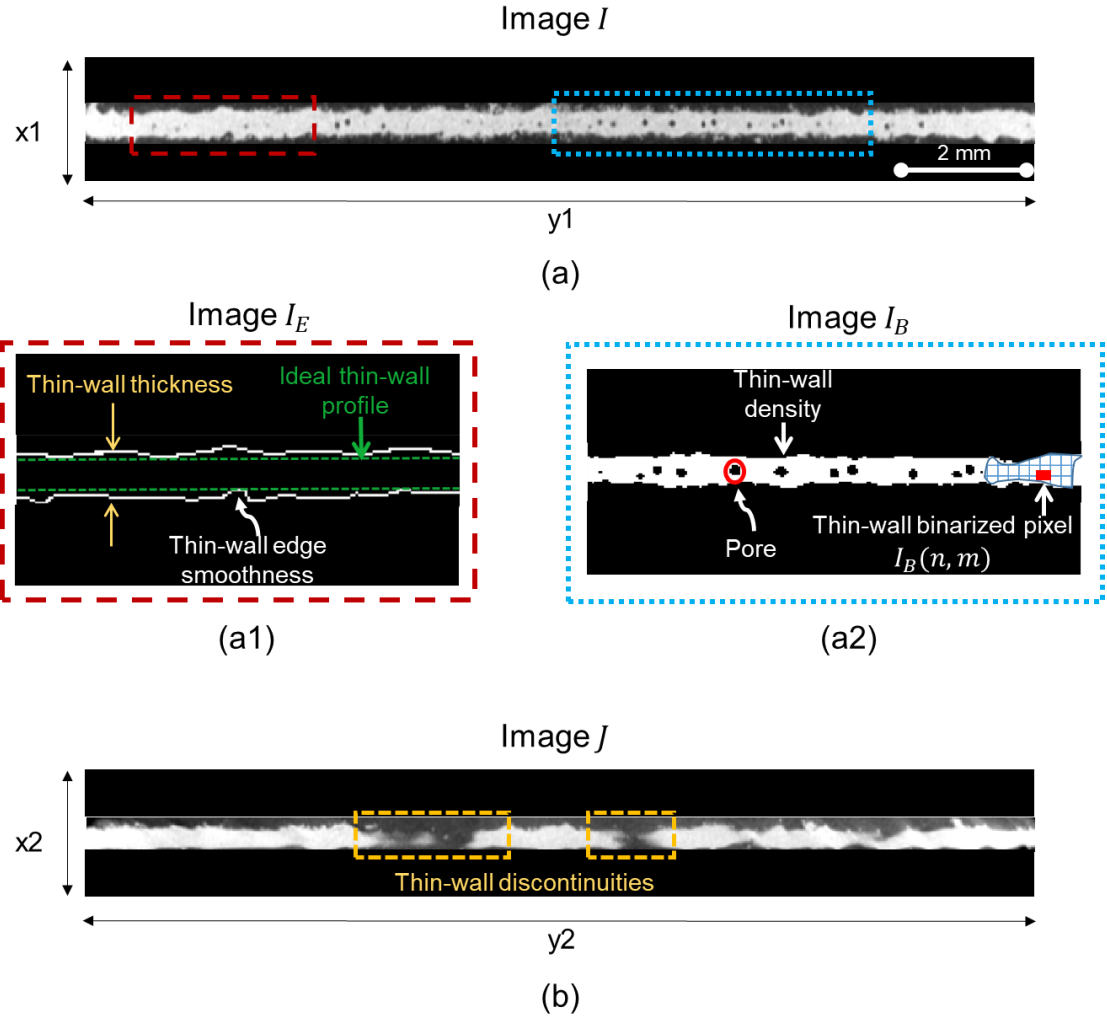


Figure 4-4: Thin-wall features extracted from XCT scan images. (a) Thin-wall layer image (I) showing thin-wall discontinuity, and highlighting two parts of the thin-wall illustrating other defects. (b) Binarized image of a thin-wall segment (B_S) representing thin-wall thickness, thin-wall edge smoothness, and ideal thin-wall profile. (c) Image of thin-wall segment (I_S) depicting thin-wall density.

A brief explanation regarding these features is provided herewith. Consider an XCT scan image I of a thin-wall of size $x1$ pixel \times $y1$ pixel (Figure 4-4(a)); the binarized segment of this image I is I_B (Figure 4-4 (a2)), and I_E is a segment that depicts the edge of the thin-wall, as shown in Figure 4-4 (a1)). The $y1$ dimension for the thin-wall image I , and $y2$ dimension of the thin-wall image J (Figure 4-4 (b)) are equal to 800 pixels and remain constant over all thin-wall images, i.e., if an image is considered to be a matrix with

each pixel representing a matrix element, the number columns remains constant. On the contrary, the x_1 and x_2 dimensions for thin-wall image I and J , vary contingent to the thin-wall thickness, but they remain constant throughout all layers for a given thin-wall, for example, $x_1 = x_2 = 36$ pixels for thin wall number 25, and $x_1 = x_2 = 32$ for thin wall number 20.

Thin-wall thickness (\bar{t}): This feature quantified the average thickness of a thin wall as follows: The edge of the thin wall as shown in Figure 4-4(a1) and Figure 4-5, was obtained by using a Canny filter on a binarized image of thin-wall segment I_B . Further, the thickness of the thin-wall segment at a given location was determined by subtracting the first non-zero entry in a column of image pixels by the last non-zero entry in the same pixel column, as represented in Figure 4-5. This procedure estimated the distance between two edges of the thin-wall at a given location. The average of the distance between two edges of the thin-wall over the length (y_1) is termed as the thickness of a thin-wall segment (\bar{t}) (Eqn. (1)).

$$\bar{t} = \frac{\sum_{i=1}^m \alpha_{1i} - \alpha_{2i}}{m} \quad (1)$$

where, α_{1i} is the first non-zero row index, α_{2i} is the second non-zero row index and m is the number of columns.

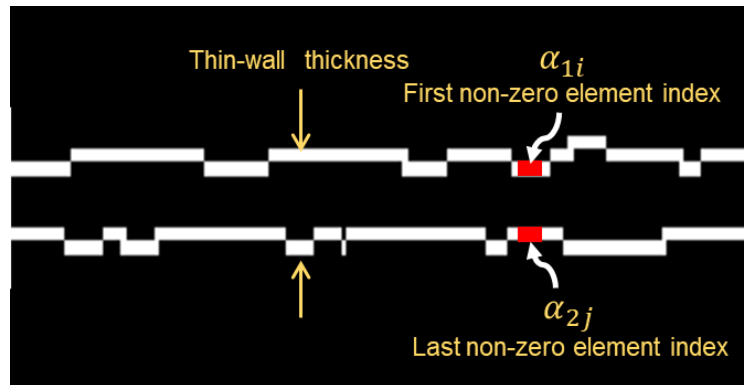


Figure 4-5: A representation of the thin-wall thickness feature. The pixels highlighted in red represent the pixels in the upper and lower edge of the thin wall.

Thin-wall density (ρ_t): The thin-wall density quantified un-melted areas or areas devoid of sufficient material that resulted in pores in an individual thin wall (Figure 4-4 (a2)) . To estimate this quantifier, the pixels within the boundary of the thin-wall image, were averaged to estimate ρ_t (Eqn. (2)).

$$\rho_t = \begin{cases} \frac{\sum_{i=1}^m \sum_{j=1}^n I(i, j)}{M} & \text{for } I > 0 \\ 0 & \text{for } I < 0 \end{cases} \quad (2)$$

where, $I(i, j)$ is the pixel within the thin-wall, and M is the number of pixels within the boundary of a thin-wall image. In Figure 4-4 (a2), a pixel in a thin-wall image is shown.

Thin-wall edge smoothness (σ_s): This feature represented the degree of smoothness of the thin-wall XCT scan image boundary. The non-zero linear row indices of the upper edge (α_{1i}) and lower edge (α_{2i}) of the thin wall, as shown in Figure 4-5, were recorded. The degree of smoothness of a thin-wall edge was evaluated by calculating the standard deviation of the column indices of each edge. This standard deviation was interpreted as follows: the higher the standard deviation, the lower would be the edge smoothness, and vice-versa.

The dotted-line in Figure 4-4 (a1) represents the edge of the thin-wall obtained from the computer-aided design (CAD) of the thin wall. As observed visually, the CAD thin-wall edge had constant α_1 and α_2 values, and thus it had no standard deviation. Whereas, the thin-wall edges of the XCT-scanned images had highly varying values of edge indices, which resulted in high standard deviation, and in turn poor edge smoothness.

Thin-wall discontinuity (δ): The discontinuity of a thin wall is highlighted in a yellow dotted-box in Figure 4-4 (b). If there was discontinuity in the thin-wall edge, it indicated

that the thin-wall was highly likely to fail. It was defined as the number of instances (δ) that the non-zero row indices α_{1i} and α_{2i} (from Eqn. (1)) were not detected in a thin-wall. A near-zero value of a thin-wall segment discontinuity was preferred.

The above four quantifiers for each thin-wall XCT-scan image were arranged in a matrix called the *quantifier matrix* (X^θ), for each orientation $\theta = \{0^\circ, 60^\circ, 90^\circ\}$, as shown in Figure 4-6. The quantifier matrix of each orientation angle was compared with features extracted from the CAD images of the thin walls. The features extracted from the CAD thin-wall images were considered to be ideal, and hence, the features extracted from the XCT-scan images were compared with them. The metric used for this comparison is known as the Mahalanobis-squared distance $(D_M^2)_t^\theta$ for orientation angle θ and thin-wall number $t = \{1, 2, 3, \dots, 25\}$ as shown in Eqn. (3).

The Mahalanobis-squared distance accounted for the variability in the data due to multiple quantifiers, both within and between quantifiers, with the help of the inverse of the variance-covariance matrix which is also known as the precision matrix.

$$(D_M^2)_t^\theta = (\bar{X}_t - \mu^{TW})' S^{-1} (\bar{X}_t - \mu^{TW}) \quad (3)$$

where, \bar{X}_t^θ is the mean feature vector of a particular thin-wall image t for orientation $\theta = \{0^\circ, 60^\circ, 90^\circ\}$ which is to be compared with the thin-wall features extracted from a CAD image of the thin wall. The features extracted from the CAD image are stored in μ^{TW} , and the S^{-1} is the precision matrix derived from the feature matrix of XCT scan images of a thin-wall with a particular orientation angle. The key idea is shown below in Figure 4-6.

$$X^{0^\circ} = \begin{pmatrix} \bar{t}_1 & \sigma_{s1} & \rho_{t1} & \delta_1 \\ \bar{t}_2 & \sigma_{s2} & \rho_{t2} & \delta_2 \\ \vdots & \vdots & \vdots & \vdots \\ \bar{t}_N & \sigma_{sN} & \rho_{tN} & \delta_N \end{pmatrix} \begin{matrix} \rightarrow \bar{X}_1^{0^\circ} \\ \rightarrow \bar{X}_2^{0^\circ} \\ \vdots \\ \bar{X}_N^{0^\circ} \end{matrix}$$

$$(D_M^2)_1^{0^\circ} = (\bar{X}_1 - \mu^{TW})' S^{-1} (\bar{X}_1 - \mu^{TW})$$

$$\bar{X}_1^{0^\circ} = [\bar{t}_1 \quad \sigma_{s1} \quad \rho_{t1} \quad \delta_1]$$

$$\mu^{TW} = [\bar{t}_{CAD} \quad \sigma_{S(CAD)} \quad \rho_{tCAD} \quad \delta_{CAD}]$$

Figure 4-6: A representation of the arrangement of the quantifier matrix for a thin-wall at 0° orientation angle. The features extracted from the first XCT scan thin-wall image with a particular aspect ratio and an orientation angle of 0° is represented by $\bar{X}_1^{0^\circ}$. The vector with features extracted from the CAD images of a thin-wall with a particular aspect ratio is represented by μ^{TW} .

4.2 Online Analysis of in-process powder bed images

This section details the approach adopted to detect build failure in thin walls by two-phase analysis of the in-process powder bed images: (1) the extraction of individual images of the thin wall from the noisy powder bed images, and (2) predicting the quality of these images as inputs to a convolutional neural network (CNN) which is trained to predict the build quality of the thin wall.

We initially tried to de-noise the powder bed image with the help of graph diffusion. This technique uses the heat diffusion kernel to smoothen an image, and simultaneously, preserves the edges in the image. Due to the high level of noise in the powder bed images, the edges of the thin walls were not very well-defined, because of which the graph diffusion

technique failed to work. Consequently, we used an image filtering technique to sharpen the image and negate the noisy background as depicted in Figure 4-7.

The resulting binary image had clearly demarcated edges for each of the thin walls. This step was done with the help of a linear filtering operation which is termed as convolution filter (not to be confused with a CNN). The convolutional filter (or convolutional kernel) is a weighted matrix which convolves around an image to give an output image whose pixels are a weighted sum of the input pixels. Shown below in Figure 4-7, is the convolution filter (or kernel) used in this case where, x is a variable which controls the intensity of the sharpening of the image i.e. the higher the value of x , the higher the erosion of the image.

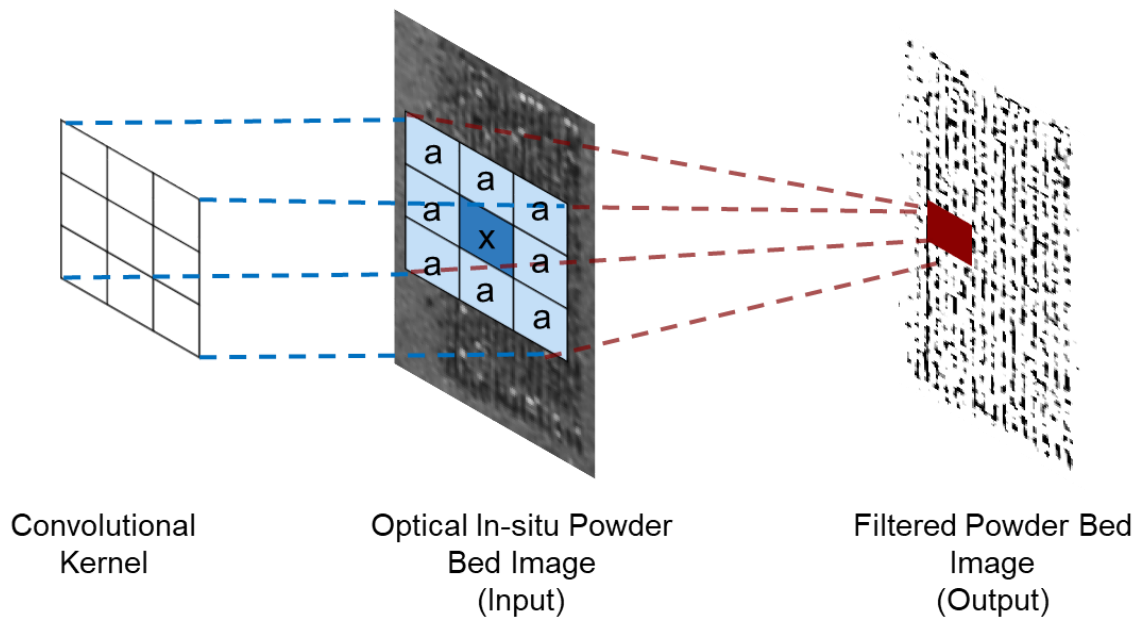


Figure 4-7: Schematic representation of image de-noising done by employing image sharpening. This technique uses a filter matrix which convolves around an image.

Convolutional neural network architecture

This section will briefly contrast the concept of the convolutional neural networks (CNN), vis-à-vis conventional feed-forward artificial neural networks (ANN) before providing mathematical details. Artificial neural networks are neurophysiologically inspired machine learning algorithms with neurons as their elementary units [36]. These neurons receive multiple inputs from either the input data or other neurons, the latter of the two being recurrent, and subsequently create an output by employing a non-linear transformation. The learning process to obtain the weights of the neurons is carried out using an algorithmic approach [37]. In a feed-forward ANN, neurons in a layer are fully connected, i.e., a neuron will be connected to all the neurons in the preceding and succeeding layer, and are independent of each other. Due to this reason, ANNs are computationally expensive for implementing back-propagation when analyzing a high volume of data, and further, ANNs do not encapsulate the spatiotemporal correlation within the data, such as images.

For example, when analyzing an image of size $200 \times 200 \times 3$, the resulting number of weights for the neurons in an ANN would be $200 \times 200 \times 3 = 120,000$. Furthermore, a large number of neurons would be required, which would then lead to a high number of parameters, thus causing overfitting. In contrast in a CNN, a neuron in one layer will only be connected to a certain number of neurons in the previous layer, thus avoiding full-connectivity, and consequently, overfitting. Accordingly, CNNs are multi-layered neural networks that have been used in detecting patterns from image pixels, such as, faces, hands, logos, text etc. [38, 39].

The CNN used in this work had four blocks along with a fully-connected layer, regression layer, input and output layer as seen in Figure 4-8. The input to the network was an image of a single thin-wall of size 28 pixels \times 28 pixels which was extracted from a denoised layer-wise powder bed image, and the output is the corresponding Mahalanobis-squared distance of the thin-wall at the given layer. Each block had a 2D convolution layer with a rectified linear unit (ReLU), a batch normalization layer, and an average pooling layer.

Convolutional layer

The convolutional layer extracts features from an image by learning various convolving filters [38]. In this CNN architecture, we used an increasing number of filters in each convolutional layers to extract complex features from the images. A filter, is an $f \times f$ matrix, which convolves around an image and creates a feature map by performing a dot product operation on the input image, as shown in Figure 4-9. The manner in which the filter convolves over the input image is determined by a hyper-parameter called *stride*. Figure 4-9 (b1), is an illustration of a filter sliding over an image with stride set to 1. To preserve the dimensions of the images being convolved, the images are padded with zeros, i.e. the images are surrounded by zeros, before the convolution operation, and this hyper-parameter is called *padding*.

The CNN used in this thesis had four blocks, and each block had a convolutional layer in it, as shown in Figure 4-8 [37]. As the network got deeper, the number of filters in each convolutional layer increased to extract high-level features from the image. It is seen in Figure 4-11 that the input image had a depth of 1 as it is a grayscale image, but the first convolution layer had depth of 8 filters. The depth of a layer was a function of the number

of filters employed in a convolution layer, and in accordance, the last convolution layer in block 4 had a depth of 32 filters.

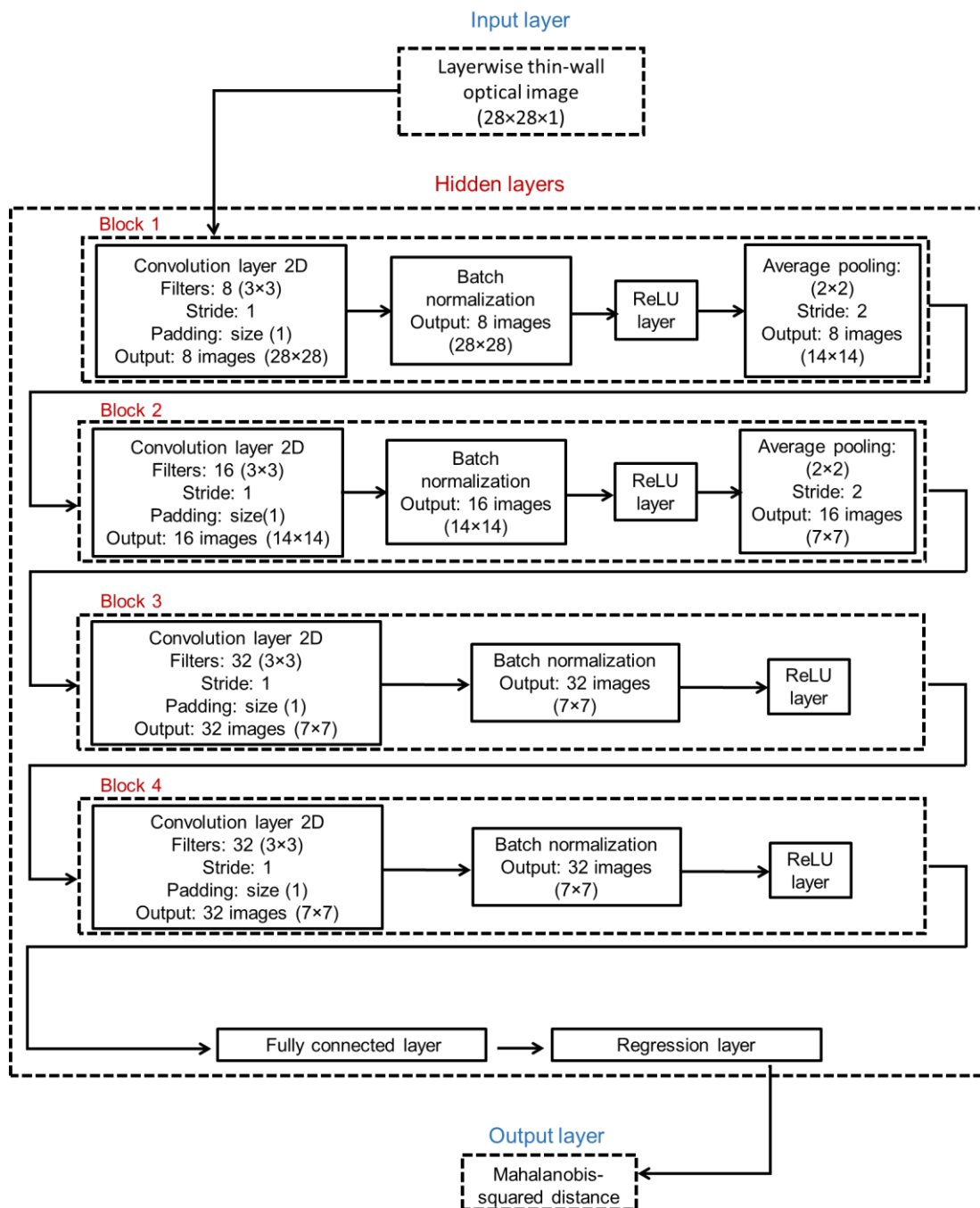


Figure 4-8: Flow-chart of the architecture of the convolutional neural network employed in this thesis to predict Mahalanobis-squared distance.

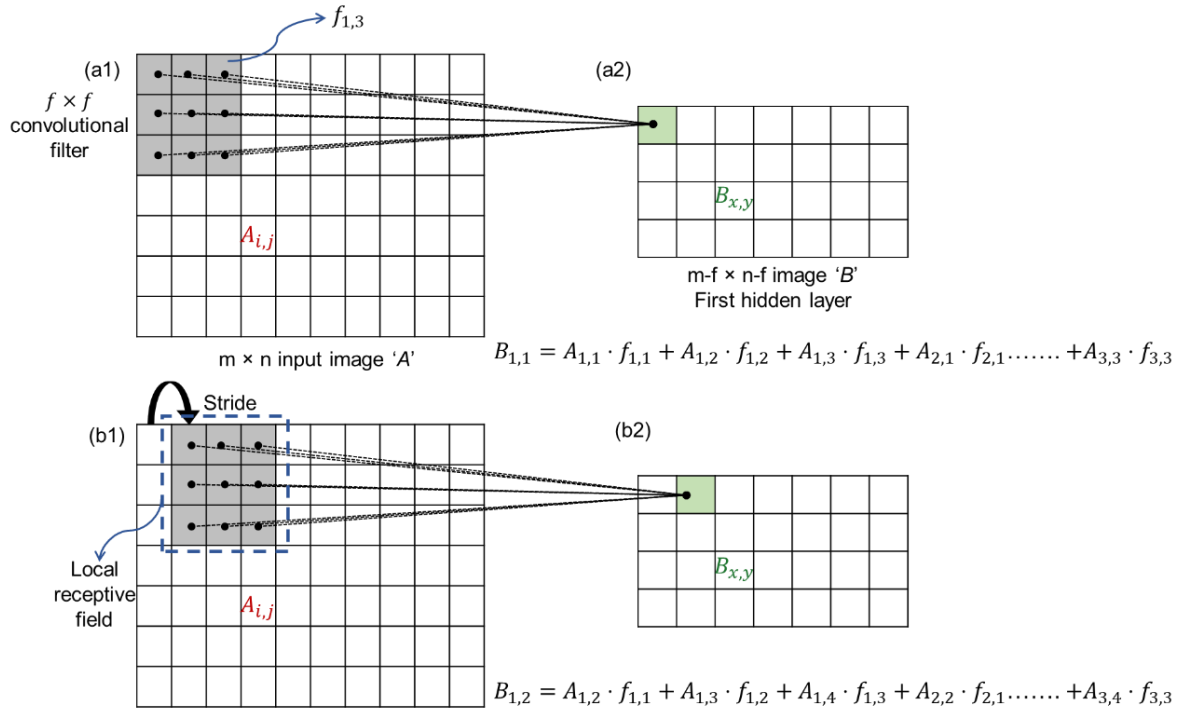


Figure 4-9: Schematic representation of convolution operation.

Batch normalization layer

The input given to a neural network is normalized, i.e. it has zero mean and unit variance, and this is done to quicken the learning process of the network. When the input variables of a network have extremely varying ranges, for example, one variable has a range of 1-1000, whereas the second one has a range of 1-2, the network parameters will have correspondingly wide ranges. This leads to a wide cost function in the direction of the variable with a wide range as this variable contributes more towards learning of the network. Due to this imbalance in the variables and the resulting elongated cost function, it becomes cumbersome to train a network. On the contrary, a neural network with normalized inputs has a circular cost function resulting in increased ease and speed of training. Likewise, it is advisable in deep neural networks to normalize the input to every layer of the network, with the help of a technique called batch normalization [40].

When updating weights in one layer in a deep neural network, it is assumed that the layer's inputs will remain constant. However, the distribution of the input might change every time the weights are updated, as the previous layer parameters are updated as well. In deep models, even small changes in earlier layers amplify drastically in the later layer, which significantly changes the input distribution to the later layers as well, making it hard for them to adapt to the changes, and thus, hindering convergence. This phenomenon is referred to as internal covariate shift, and batch normalization layers are employed in a deep neural network to prevent it.

In batch normalization, the inputs are firstly normalized to zero mean and unit variance as shown below in Eqn. (4)-(6). This normalization is not performed on the whole input population at once, but is done on the inputs in batches [40].

$$\mu_B = \frac{1}{n} \sum_{k=1}^n a_k \quad (4)$$

$$\sigma_B^2 = \frac{1}{n} \sum_{k=1}^n (a_k - \mu_B)^2 \quad (5)$$

$$\widehat{a}_k = \frac{a_k - \mu_B}{\sqrt{\sigma_B^2}} \quad (6)$$

where, μ_B and σ_B^2 are the mean and variance of the batch, respectively, \widehat{a}_k is the normalized input value, and n is the batch size. Subsequently, the normalized inputs (\widehat{a}_k) are scaled and shifted to have an arbitrary mean and variance of the input distribution (Eqn. (7)).

$$o_k = \delta \widehat{a}_k + \alpha \quad (7)$$

where, o_k is an output of the batch normalization layer, and accordingly is the input to the activation (ReLU) layer, δ is the scaling factor, and α is the shifting factor; and these factors facilitate in randomizing the mean and variance of the batch inputs. Intuitively, it can be argued that these factors nullify the effect of normalization, as prior to batch normalization, the data had random mean and variance. Taking a step backward, we can see that the mean and variance without batch normalization are dependent on excessively high numbers of parameters, such as weights and biases of each neuron, activations, etc., but in the case of batch normalization they are dependent only on the two scaling and shifting factors which are trainable and learnable by the network.

When testing the network, the μ_B and σ_B^2 are not available, so the estimation of the population expectation and population variance are calculated as follows.

$$E_{k+1}[x] = \delta E_k[x] + (1 - \alpha) \mu_B \quad (8)$$

$$Var_{k+1}[x] = \delta Var_k[x] + (1 - \alpha) \sigma_B^2 \quad (9)$$

In our neural network architecture used in this work, a batch normalization layer was employed, as shown in Figure 4-8.

Rectified linear unit (ReLU) layer

The rectified linear unit (ReLU) is an activation function (non-linearity) which sets all negative values to zero [41]. It is formally given as follows.

$$f(x) = \begin{cases} x & \text{if } x \geq 0 \\ 0 & \text{if } x < 0 \end{cases} \quad (10)$$

The ReLU layers are preferred over other activation functions, such as the sigmoid function and hyperbolic tangent (tanh) function, because it is found that the ReLU layers significantly accelerate the convergence of the stochastic gradient descent, i.e., the ability

of the network to reach its cost/loss function minima [42]. Further, the ReLU layers are computationally inexpensive as they only involve thresholding an activation matrix, whereas on the contrary, the sigmoid and tanh functions need heavy computations. Also, the ReLU layers avoid vanishing the gradient which is quite evident in the hyperbolic tangent function and sigmoid. Neural networks that are trained with the help of gradient-based learning method and the back-propagation method often encounter the vanishing gradient problem [41]. These methods provide the neurons with updated weights that are proportional to the partial derivative of the error function (the difference between the value predicted by the network and the actual value) with respect to the current weights of the neurons in each training iteration. When activation functions such as the tanh function and sigmoid function are used, the vanishing gradient problem is observed as they have gradients in the range $(0, 1)$, and in the backpropagation method the gradients are computed by the chain rule. This results in the multiplication of n of these small numbers to calculate gradients of the initial layers in an n -layer network, which means that the gradient (error signal) diminishes exponentially with n , thus leading to the initial layers being trained slowly. In other words, vanishingly small gradients prevent the training of the network as the weights remain constant after every iteration. In our network, we have used the ReLU layer in each block after the batch normalization layer as seen in Figure 4-8.

Average pooling layer

The average pooling layers are used to down-sample the spatial arrangement of an image (Figure 4-11) to reduce the computation, and also to avoid over-fitting, i.e., the network gets highly fitted to the training data, and cannot adapt to the inputs of the testing data, thus performing poorly. The spatial reduction is performed as it is sufficient to know

the relative position of features with respect to other features, rather than knowing the exact feature location. Similar to a convolution layer, in an average pooling layer, filters of a given size move around an image in a non-overlapping manner, resulting in a single value which is the average of all values of the image in the given filter size (Figure 4-10) [38]. Along with filter size, another hyper-parameter that the average pooling layer employs is stride, which dictates the movement of the filter over the image. The layer individually operates on each of the depth slice of the input image, thus conserving that dimension (Figure 4-11), and also the feature data accumulated from various filters.

In this work, we used average pooling layers in the first two blocks as seen in Figure 4-8. This layer was not used in the succeeding layers to avoid significant reduction in the spatial dimensions of the image resulting in feature data loss. The pooling layers used a filter size of 2×2 , and a stride of 2 in both blocks (Figure 4-10). This resulted in the reduction of the input image size from 28×28 , to 7×7 at the end of the second block.

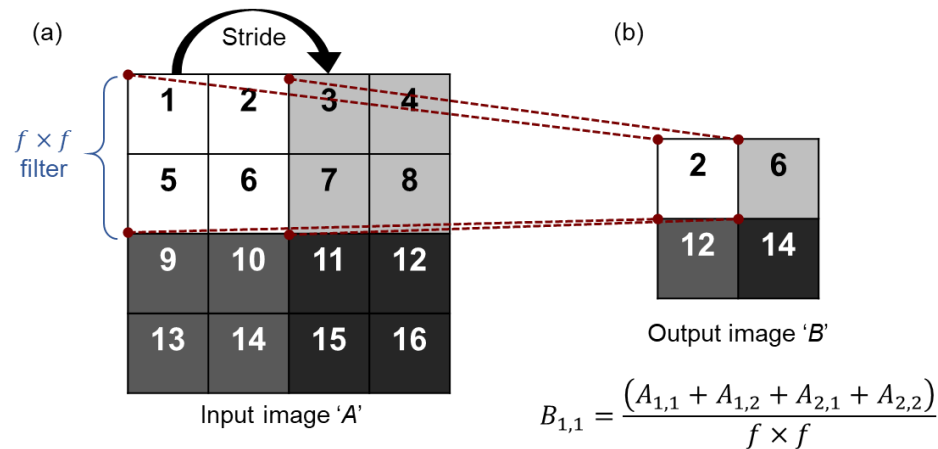


Figure 4-10: Schematic representation of an average pooling operation.

Fully connected layer

In a fully connected layer, all the neurons in the adjacent layers are pairwise connected to each other, but neurons in the same layers are independent of each other. Unlike a

convolutional layer, the fully connected layer is a one-dimensional vector which has all the activations of the previous layer, as seen in Figure 4-11. Due to this drastic change in dimension, fully-connected layers are placed at the end of the network, and convolution layers cannot be placed after them. Each convolution layer identifies features such as, lines, edges, curves, and shapes, with the help of various filters, the fully-connected layer fuses these features together and comes up with a prediction close to the desired output. The fully-connected layer in this network had 1568 inputs in it from the previous non-linearized (ReLU) convolution layer and had a single output which was passed to the regression layer. The mean squared error (MSE) is the difference between the predicted output and the desired output. In this regression layer, based on this MSE, weights of all neurons in the network were updated to obtain the optimum minima of the MSE. For training the network, values of hyper-parameters like maximum epochs (maximum number of iterations), and the learning rate for weights, were heuristically set to achieve the lowest value of MSE. The value of maximum epochs was chosen in such a way that it was avoided under the network training, and also avoided over-fitting. Similarly, the learning rate of weights, which is a hyper-parameter that controls the adjustment of the weights with respect to the cost function gradient, was set to an optimum level so as to preserve the network speed, and also not to miss out on a local minima of the cost function.

For training the convolutional neural network, the input used was an individual thin-wall extracted from de-noised, layer-wise powder bed images, and the output was the corresponding Mahalanobis-squared distance of the fin obtained from the XCT-scan image analysis. The data was allocated in the following manner: 75% for training the network (randomly selected), and 25% for testing the network.

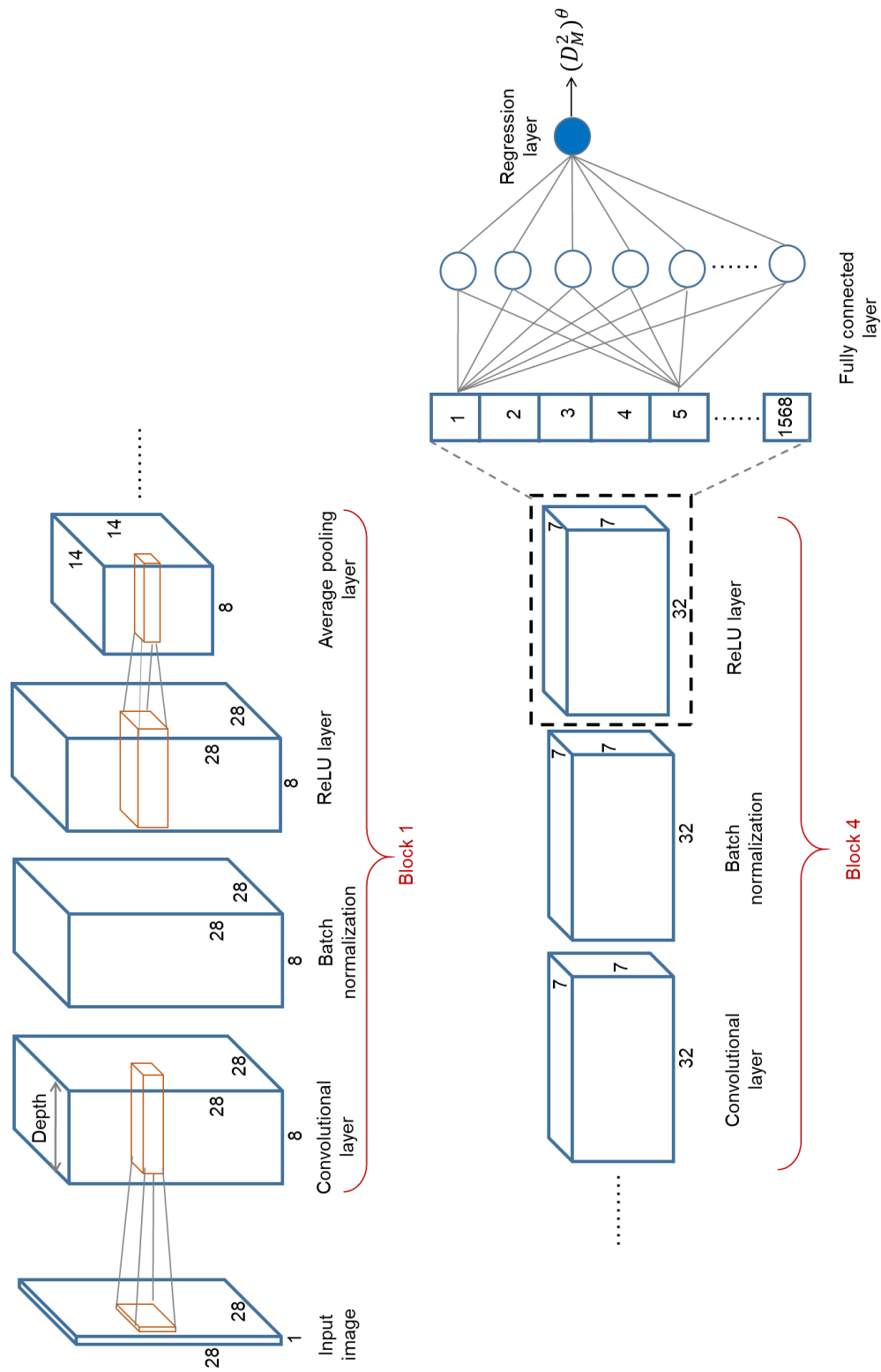


Figure 4-11: The schematic representation of the convolutional neural network architecture

CHAPTER 5 RESULTS

This chapter reports the results from the XCT scan image analysis described in section 4.1, in terms of the geometric design rules for thin-wall structures, and in-process monitoring of thin walls using the CNN described in section 4.2.

5.1 Geometric design rules for thin-walls based on offline XCT scan images

For a fixed aspect ratio, the thin walls oriented at 0° to the re-coater direction, had a superior build quality. In other words, when the long edge of the thin wall was parallel to the direction in which the re-coater moves, the thin-wall feature tended to build with fewer flaws compared to those thin-wall structures that were built with the broadside of the thin-wall exposed to the re-coater. At an orientation of 90° , where the broadside of the thin wall was perpendicular to the re-coater motion, the build quality was worst. For example, consider Figure 5-1 (a); thin-wall built at orientation angle of 0° at layer number 22 was built without any discernable flaws, whereas those built at 60° and 90° depicted non-smooth edges and discontinuity. Furthermore, at layer number 25, irrespective of the orientation angle, the thin walls have completely collapsed.

In contrast, for a smaller aspect ratio, the thin wall shown in Figure 5-1 (b), a discernable difference in the thin-wall quality at the three different orientations was seen only at layer number 35. Here, the thin wall built at 0° , as well as at 60° had distinctly better geometric integrity, compared to the thin wall built at 90° . An observation drawn from Figure 5-1 is that a threshold value of 15 can be arbitrarily set for the Mahalanobis-squared distance, beyond which the thin-wall quality is typically poor. We note that this observation is specific to this particular work.

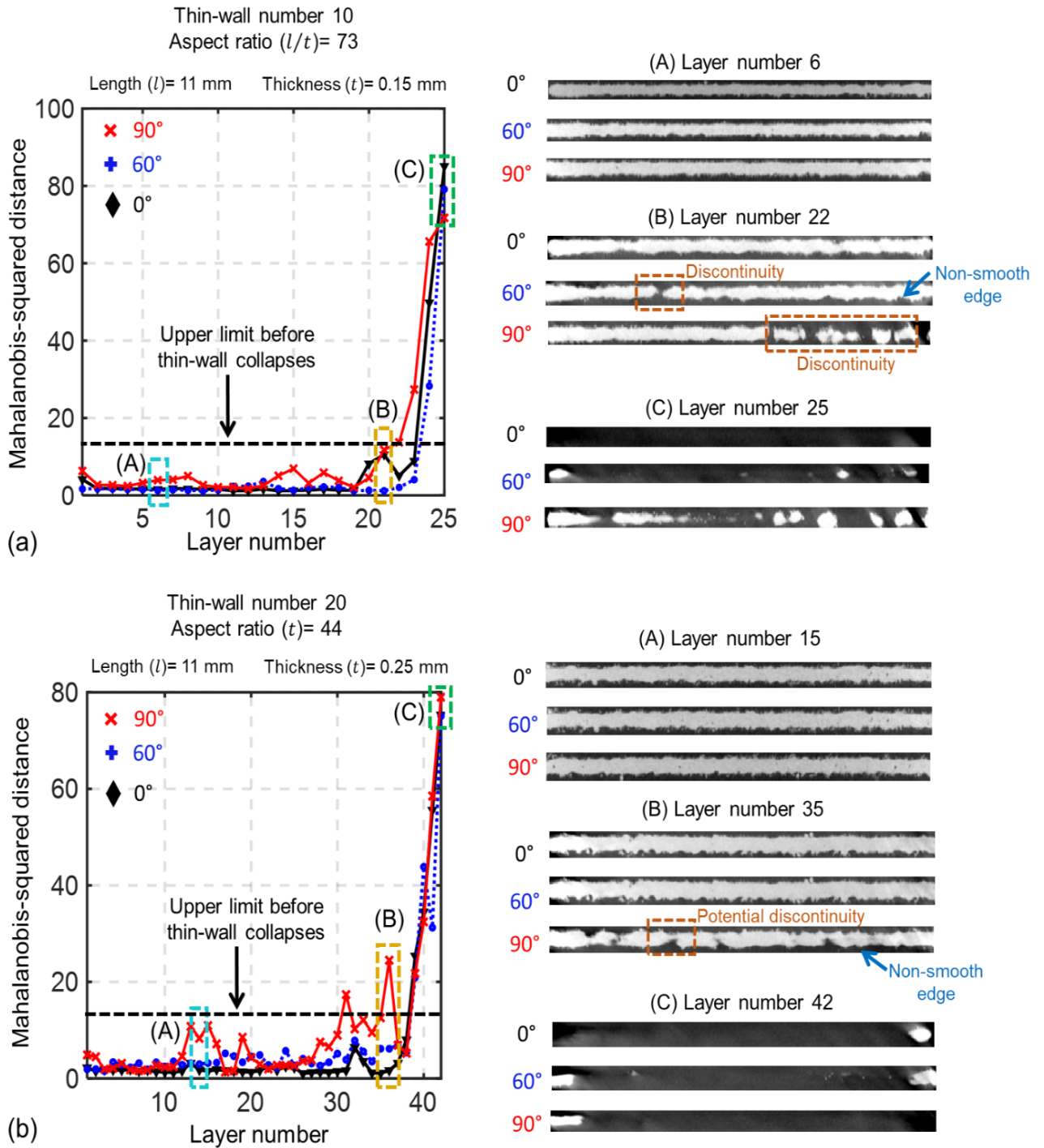


Figure 5-1: Mahalanobis-squared distance for different orientations (θ) of different thin walls. (a) Thin wall number 10, with aspect ratio (l/t) of 73, i.e., length $l= 11$ mm and thickness $t= 0.15$ mm. (b) Thin wall number 20, with aspect ratio (l/t) of 44, i.e., length $l= 11$ mm and thickness $t= 0.25$ mm.

Next, we have summarized the influence of the aspect ratio in Figure 5-2, which maps the build height versus the aspect ratio averaged across all orientation angles and recommended build height to achieve good geometrical integrity. Figure 5-3 depicts this information in greater detail with the recommended height for building thin-walls with good geometrical integrity, and the height at which thin walls collapse with respect to a given orientation and aspect ratio.

The geometric design rules can be generalized as follows.

- a) Avoid building thin walls below 0.15 mm thickness, i.e., aspect ratio (l/t) above 73, because they tend to collapse.
- b) Avoid building thin walls at angles inclined to the re-coater blade. In other words, avoid presenting the broadside of the thin wall to the re-coater.
- c) The maximum recommended height for a thin wall of thickness t is approximately $9 \times t$.

The design rules formulated from this work are summarized and pictorially represented in Figure 5-4.

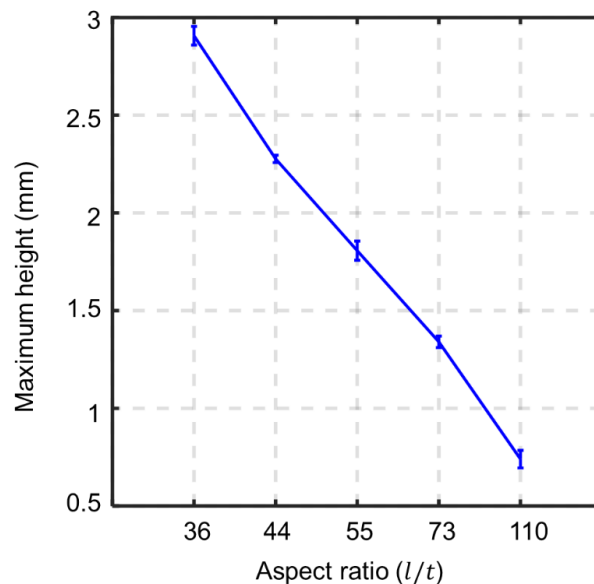


Figure 5-2: Maximum recommended height to build thin walls of good geometrical integrity with respect to aspect ratio (l/t).

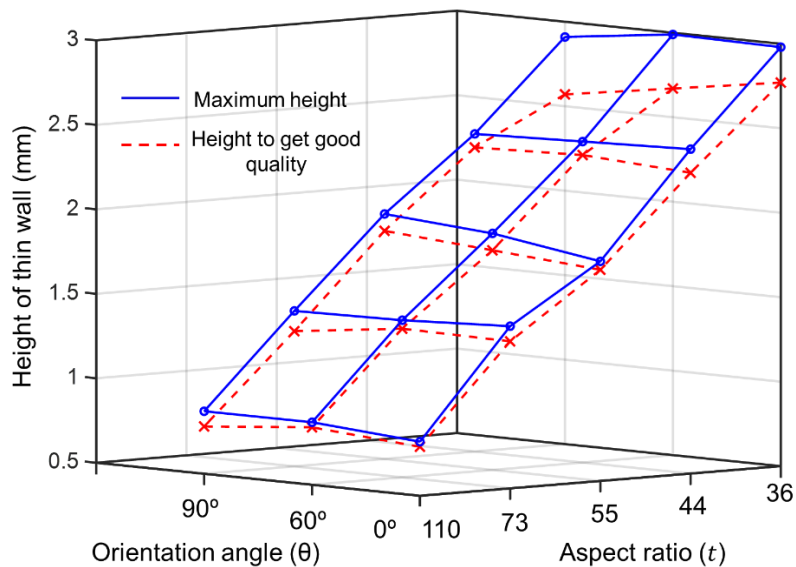
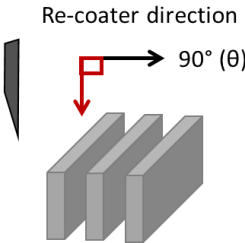
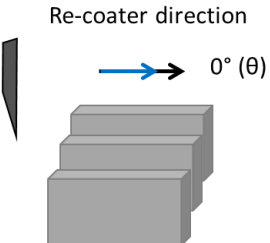
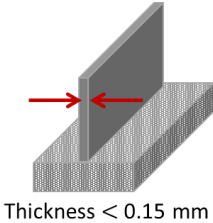
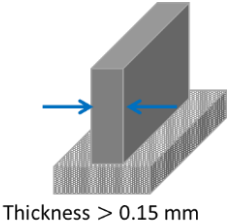


Figure 5-3: Maximum build height of thin walls to get good geometrical integrity, and height at which thin walls collapse, with respect to aspect ratio and orientation angles.

Description	Unsuitable	Suitable
<p>The orientation angle (θ) of 90° should be avoided while building thin wall structures.</p>		
<p>The aspect ratio (l/t) of a thin wall should not exceed 73 (11 mm / 0.15 mm).</p>	 <p>Thickness < 0.15 mm</p>	 <p>Thickness > 0.15 mm</p>

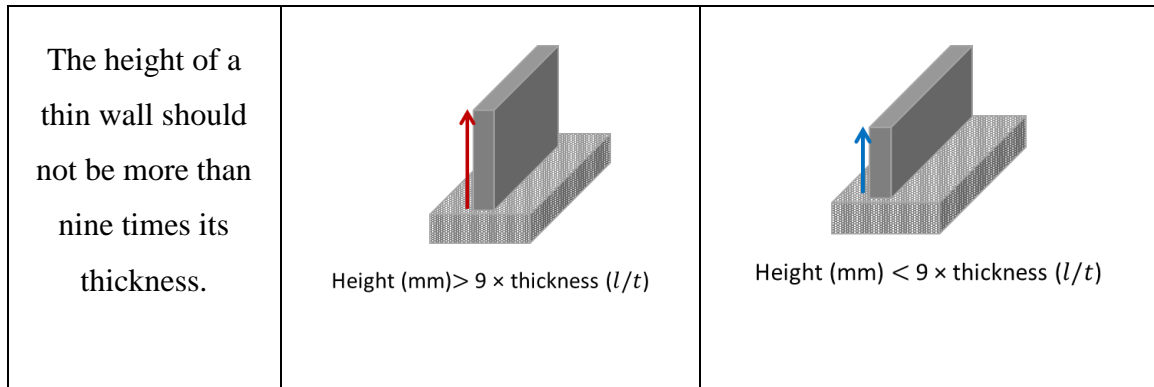


Figure 5-4: Summary and pictorial description of the geometric design rules formulated from this work for thin wall features built using laser powder bed fusion additive manufacturing process.

5.2 Results from in-process powder bed image analysis

In this section, we used the online layer-by-layer image data to detect the onset of defects in a thin-wall part. The key idea was to apply the convolutional neural network (CNN) described in Chapter 4 to predict the Mahalanobis-squared distance as a surrogate or derived measure of build quality. The network training procedure and network architecture are explained in great detail in section 4.2.

Figure 5-5 shows the representative results for thin wall number 23 under three different orientations. These results indicated that the CNN derived Mahalanobis-squared distance results, closely tracked those obtained using XCT scan image analysis of the thin wall. As a consequence, instead of expensive post-process XCT scan measurements, the in-process image data could be used for detecting process defects in laser powder bed fusion. As a quantitative measure to ascertain the closeness between the observed and CNN-predicted Mahalanobis-squared distance trends, we used the Pearson coefficient. For trends shown in Figure 5-5, the Pearson correlation coefficient ranges from 80.26 % to 98.89 %.

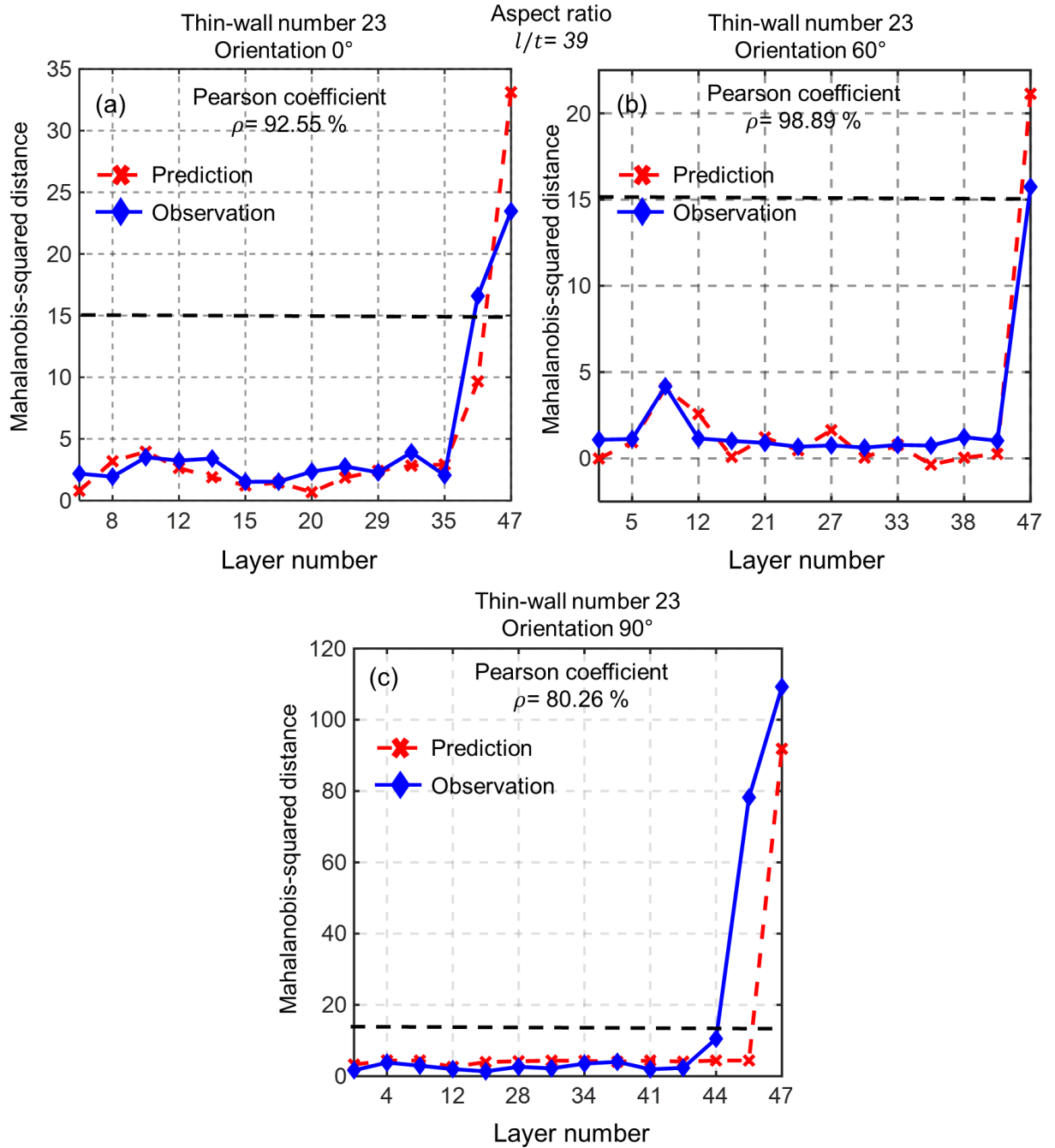


Figure 5-5: Mahalanobis-squared distance prediction via CNN regression for thin wall number 23 ($l/t = 39$, length = 11 mm, thickness = 0.28 mm) with (a) 0° orientation, (b) 60° orientation and (c) 90° orientation.

CHAPTER 6 – CONCLUSIONS AND FUTURE WORK

This work investigated the quality of thin-wall parts made using the laser powder bed fusion (LPBF) process as a function of their build orientation and aspect ratio (length-to-thickness ratio, l/t). Furthermore, in-process optical image data of the powder bed was acquired with the aim of detecting build flaws. Specific contributions from this work are as follows:

- 1) The effect of aspect ratio and wall thickness was quantified by extracting statistical features from the offline X-ray computed tomography (XCT) scan images of thin-wall parts. The following results are reported herein from the perspective of the design of additive manufacturing (AM). The number of layers (vertical height) of a thin-wall part that can be built without damage was contingent on its aspect ratio and build orientation. It is recommended that a thin wall be built with 0° orientation with the re-coater blade. In other words, the broadside of the fin should not, as far as possible, face the re-coater direction. The maximum vertical height of the thin wall should be less than 9 times its thickness.
- 2) Four quantifiers were defined to characterize the geometric integrity of the thin wall. These quantifiers were aggregated in terms of the Mahalanobis-squared distance, which was positively correlated with the visual quality of the thin-wall.
- 3) From the in-process quality monitoring vista, we trained a convolutional neural network (CNN) to predict the thin-wall quality (in terms of the Mahalanobis-squared distance) based on in-process optical images of the powder bed. For the representative cases tested, the Pearson correlation coefficient (ρ) between the Mahalanobis-squared

distance measured from the XCT scan signatures, and the CNN-derived Mahalanobis-squared distance was in the range of 80.26 % to 98.89 %.

This work thus makes a foray into deriving quantitative rules for design of laser powder bed fusion parts, specifically thin-wall structures. Furthermore, we have forwarded a feature-free deep learning approach to detect build flaws in laser powder bed fusion parts. Consequently, this work makes an effort to complete the following link from the LPBF perspective: Part design \rightarrow In-process data \rightarrow Build quality. However, the following question remain to be addressed, which we will endeavor to answer in our future forays in the area:

- 1) What is the generalizability of the design rules proposed for variation in material and thin-wall structures built with different process conditions such as, laser power and velocity?
- 2) How do the proposed design rules for thin walls carry over to internal thin-wall features, and thin walls with overhang geometries?
- 3) What is the ability of the CNN proposed in this work to apply to other types of features through transfer learning?

REFERENCES CITED

- [1] Imani, F., Gaikwad, A., Montazeri, M., Rao, P., Yang, H., and Reutzel, E., 2018, "Process Mapping and In-Process Monitoring of Porosity in Laser Powder Bed Fusion Using Layerwise Optical Imaging," *Journal of Manufacturing Science and Engineering*, 140(10), pp. 101009-101009-101014.doi:[10.1115/1.4040615](https://doi.org/10.1115/1.4040615)
- [2] Montazeri, M., and Rao, P., 2018, "Sensor-Based Build Condition Monitoring in Laser Powder Bed Fusion Additive Manufacturing Process Using a Spectral Graph Theoretic Approach," *Journal of Manufacturing Science and Engineering*, 140(9), pp. 091002-091002-091016.doi:[10.1115/1.4040264](https://doi.org/10.1115/1.4040264)
- [3] Yao, B., Imani, F., Sakpal, A. S., Reutzel, E., and Yang, H., 2018, "Multifractal analysis of image profiles for the characterization and detection of defects in additive manufacturing," *Journal of Manufacturing Science and Engineering*, 140(3), p. 031014.doi:[10.1115/1.4037891](https://doi.org/10.1115/1.4037891)
- [4] Sames, W. J., List, F. A., Pannala, S., Dehoff, R. R., and Babu, S. S., 2016, "The metallurgy and processing science of metal additive manufacturing," *International Materials Reviews*, 61(5), pp. 315-360.doi:[10.1080/09506608.2015.1116649](https://doi.org/10.1080/09506608.2015.1116649)
- [5] DebRoy, T., Wei, H., Zuback, J., Mukherjee, T., Elmer, J., Milewski, J., Beese, A., Wilson-Heid, A., De, A., and Zhang, W., 2018, "Additive manufacturing of metallic components—process, structure and properties," *Progress in Materials Science*, 92, pp. 112-224.doi:<https://doi.org/10.1016/j.pmatsci.2017.10.001>
- [6] Frazier, W. E., 2014, "Metal Additive Manufacturing: A Review," *Journal of Materials Engineering and Performance*, 23(6), pp. 1917-1928.doi:[10.1007/s11665-014-0958-z](https://doi.org/10.1007/s11665-014-0958-z)
- [7] Zwier, M. P., and Wits, W. W., 2016, "Design for additive manufacturing: Automated build orientation selection and optimization," *Procedia CIRP*, 55, pp. 128-133.doi:<https://doi.org/10.1016/j.procir.2016.08.040>.
- [8] Gao, W., Zhang, Y., Ramanujan, D., Ramani, K., Chen, Y., Williams, C. B., Wang, C. C., Shin, Y. C., Zhang, S., and Zavattieri, P. D., 2015, "The status, challenges, and future of additive manufacturing in engineering," *Computer-Aided Design*, 69, pp. 65-89.doi:<https://doi.org/10.1016/j.cad.2015.04.001>
- [9] Rao, P. K., Kong, Z., Duty, C. E., Smith, R. J., Kunc, V., and Love, L. J., 2015, "Assessment of Dimensional Integrity and Spatial Defect Localization in Additive Manufacturing Using Spectral Graph Theory," *Journal of Manufacturing Science and Engineering*, 138(5), pp. 051007-051007-051012.doi:[10.1115/1.4031574](https://doi.org/10.1115/1.4031574)
- [10] Grasso, M., and Colosimo, B. M., 2017, "Process defects and in situ monitoring methods in metal powder bed fusion: a review," *Measurement Science and Technology*, 28(4), p. 044005.doi:<https://doi.org/10.1088/1361-6501/aa5c4f>
- [11] Spears, T. G., and Gold, S. A., 2016, "In-process sensing in selective laser melting (SLM) additive manufacturing," *Integrating Materials and Manufacturing Innovation*, 5(1), p. 2.doi:[10.1186/s40192-016-0045-4](https://doi.org/10.1186/s40192-016-0045-4)

- [12] Gong, H., 2013, "Generation and detection of defects in metallic parts fabricated by selective laser melting and electron beam melting and their effects on mechanical properties," Ph.D., University of Louisville.
- [13] Dunbar, A., Denlinger, E., Heigel, J., Michaleris, P., Guerrier, P., Martukanitz, R., and Simpson, T., 2016, "Development of experimental method for in situ distortion and temperature measurements during the laser powder bed fusion additive manufacturing process," *Additive Manufacturing*, 12, pp. 25-30.[doi:https://doi.org/10.1016/j.addma.2016.04.007](https://doi.org/10.1016/j.addma.2016.04.007)
- [14] Dunbar, A. J., Denlinger, E. R., Gouge, M. F., Simpson, T. W., and Michaleris, P., 2017, "Comparisons of laser powder bed fusion additive manufacturing builds through experimental in situ distortion and temperature measurements," *Additive Manufacturing*, 15, pp. 57-65.[doi:https://doi.org/10.1016/j.addma.2017.03.003](https://doi.org/10.1016/j.addma.2017.03.003)
- [15] Scime, L., and Beuth, J., 2018, "Anomaly detection and classification in a laser powder bed additive manufacturing process using a trained computer vision algorithm," *Additive Manufacturing*, 19, pp. 114-126.[doi:https://doi.org/10.1016/j.addma.2017.11.009](https://doi.org/10.1016/j.addma.2017.11.009)
- [16] Scime, L., and Beuth, J., 2018, "A multi-scale convolutional neural network for autonomous anomaly detection and classification in a laser powder bed fusion additive manufacturing process," *Additive Manufacturing*, 24, pp. 273-286.[doi:https://doi.org/10.1016/j.addma.2018.09.034](https://doi.org/10.1016/j.addma.2018.09.034)
- [17] Yao, B., Imani, F., and Yang, H., 2018, "Markov Decision Process for Image-guided Additive Manufacturing," *IEEE Robotics and Automation Letters*, pp. 2792-2798.[doi:https://doi.org/10.1109/LRA.2018.2839973](https://doi.org/10.1109/LRA.2018.2839973)
- [18] Yao, B., and Yang, H., 2018, "Constrained Markov Decision Process Modeling for Sequential Optimization of Additive Manufacturing Build Quality," *IEEE Access*, pp. 54786-54794.[doi:https://doi.org/10.1109/ACCESS.2018.2872391](https://doi.org/10.1109/ACCESS.2018.2872391)
- [19] Hague *, R., Mansour, S., and Saleh, N., 2004, "Material and design considerations for rapid manufacturing," *International Journal of Production Research*, 42(22), pp. 4691-4708.[doi:10.1080/00207840410001733940](https://doi.org/10.1080/00207840410001733940)
- [20] Rosen, D. W., 2014, "Research supporting principles for design for additive manufacturing," *Virtual and Physical Prototyping*, 9(4), pp. 225-232.[doi:10.1080/17452759.2014.951530](https://doi.org/10.1080/17452759.2014.951530)
- [21] Atzeni, E., and Salmi, A., 2012, "Economics of additive manufacturing for end-usable metal parts," *The International Journal of Advanced Manufacturing Technology*, 62(9), pp. 1147-1155.[doi:10.1007/s00170-011-3878-1](https://doi.org/10.1007/s00170-011-3878-1)
- [22] Ponche, R., Kerbrat, O., Mognol, P., and Hascoet, J.-Y., 2014, "A novel methodology of design for Additive Manufacturing applied to Additive Laser Manufacturing process," *Robotics and Computer-Integrated Manufacturing*, 30(4), pp. 389-398.[doi:https://doi.org/10.1016/j.rcim.2013.12.001](https://doi.org/10.1016/j.rcim.2013.12.001)
- [23] Bendsoe, M., and Sigmund, O., 2004, *Topology Optimization: Theory, Methods, and Applications*, Springer.

- [24] Kranz, J., Herzog, D., and Emmelmann, C., 2015, "Design guidelines for laser additive manufacturing of lightweight structures in TiAl6V4," *Journal of Laser Applications*, 27(S1), p. S14001.doi:<https://doi.org/10.2351/1.4885235>
- [25] Thomas, D., 2009, "The development of design rules for selective laser melting," Ph.D. Dissertation, University of Wales.
- [26] Adam, G. A. O., and Zimmer, D., 2014, "Design for Additive Manufacturing—Element transitions and aggregated structures," *CIRP Journal of Manufacturing Science and Technology*, 7(1), pp. 20-28.doi:<https://doi.org/10.1016/j.cirpj.2013.10.001>
- [27] Tapia, G., and Elwany, A., 2014, "A Review on Process Monitoring and Control in Metal-Based Additive Manufacturing," *Transactions of the ASME, Journal of Manufacturing Science and Engineering*, 136(6), p. 060801.doi:[10.1115/1.4028540](https://doi.org/10.1115/1.4028540)
- [28] Everton, S. K., Hirsch, M., Stravroulakis, P., Leach, R. K., and Clare, A. T., 2016, "Review of in-situ process monitoring and in-situ metrology for metal additive manufacturing," *Materials & Design*, 95, pp. 431-445.doi:<https://doi.org/10.1016/j.matdes.2016.01.099>
- [29] Mani, M., Lane, B., Donmez, A., Feng, S., Moylan, S., and Fesperman, R., 2015, "NISTIR 8036: Measurement Science Needs for Real-time Control of Additive Manufacturing Powder Bed Fusion Processes," NIST, Gaithersburg, MD.
- [30] Nassar, A., Spurgeon, T., and Reutzel, E., 2014, "Sensing defects during directed-energy additive manufacturing of metal parts using optical emissions spectroscopy," *Solid Freeform Fabrication Symposium Proceedings*,
- [31] Gobert, C., Reutzel, E. W., Petrich, J., Nassar, A. R., and Phoha, S., 2018, "Application of supervised machine learning for defect detection during metallic powder bed fusion additive manufacturing using high resolution imaging," *Additive Manufacturing*, 21, pp. 517-528.doi:<https://doi.org/10.1016/j.addma.2018.04.005>
- [32] Abdelrahman, M., Reutzel, E. W., Nassar, A. R., and Starr, T. L., 2017, "Flaw detection in powder bed fusion using optical imaging," *Additive Manufacturing*, 15, pp. 1-11.doi:<https://doi.org/10.1016/j.addma.2017.02.001>
- [33] Montazeri, M., Yavari, R., Rao, P., and Boulware, P., 2018, "In-Process Monitoring of Material Cross-Contamination Defects in Laser Powder Bed Fusion," *Journal of Manufacturing Science and Engineering*, 140(11), pp. 111001-111001-111019.doi:[10.1115/1.4040543](https://doi.org/10.1115/1.4040543)
- [34] Craeghs, T., Clijsters, S., Kruth, J. P., Bechmann, F., and Ebert, M. C., 2012, "Detection of Process Failures in Layerwise Laser Melting with Optical Process Monitoring," *Physics Procedia*, 39, pp. 753-759.doi:[10.1016/j.phpro.2012.10.097](https://doi.org/10.1016/j.phpro.2012.10.097)
- [35] Chen, R., Imani, F., Reutzel, E. W., and Yang, H., 2019, "From Design Complexity to Build Quality in Additive Manufacturing - A Sensor-based Perspective," 3(1).doi:[10.1109/LSENS.2018.2880747](https://doi.org/10.1109/LSENS.2018.2880747)
- [36] Hagan, M. T., Demuth, H. B., and Beale, M., 1997, *Neural Network Design*, PWS Publishing, Boston, MA.

- [37] Williams, J., Dryburgh, P., Clare, A., Rao, P., and Samal, A., 2018, "Defect Detection and Monitoring in Metal Additive Manufactured Parts through Deep Learning of Spatially Resolved Acoustic Spectroscopy Signals," *Smart and Sustainable Manufacturing Systems*, 2(1), pp. 204-226.[doi:10.1520/SSMS20180035](https://doi.org/10.1520/SSMS20180035)
- [38] LeCun, Y., Kavukcuoglu, K., and Farabet, C., 2010, "Convolutional networks and applications in vision," *Proceedings of 2010 IEEE International Symposium on Circuits and Systems*, pp. 253-256.[doi:10.1109/ISCAS.2010.5537907](https://doi.org/10.1109/ISCAS.2010.5537907).
- [39] Zhang, X., Zhao, J., and LeCun, Y., 2015, "Character-level convolutional networks for text classification," *Advances in Neural Information Processing Systems (NIPS 2015)*, pp. 649-657
- [40] Ioffe, S., and Szegedy, C., 2015, "Batch Normalization: Accelerating Deep Network Training by Reducing Internal Covariate Shift," *Computing Research Repository (CoRR)*.[doi:arXiv:1502.03167](https://arxiv.org/abs/1502.03167)
- [41] Glorot, X., Bordes, A., and Bengio, Y., 2011, "Deep Sparse Rectifier Neural Networks," *Proceedings of the Fourteenth International Conference on Artificial Intelligence and Statistics*, G. Geoffrey, D. David, and D. Miroslav, eds., PMLR, *Proceedings of Machine Learning Research*, pp. 315--323.
- [42] Bottou, L., 1991, "Stochastic gradient learning in neural networks," *Proceedings of Neuro-Nimes*, 91(8), p. 12

This M.S. thesis was funded by the National Science Foundation (NSF) via the following grant

CMMI: 1752069

CAREER: Smart Additive Manufacturing - Fundamental Research in Sensing, Data Science, and Modeling Toward Zero Part Defects.

